A Middle Crustal Channel of Radial Anisotropy Beneath the Northeastern Basin and Range

Justin Wilgus[1], Chengxin Jiang[1], and Brandon Schmandt[1]

[1]University of New Mexico

November 25, 2022

Abstract

A challenge in interpreting the origins of seismic anisotropy in deformed continental crust is that composition and rheology vary with depth. We investigated anisotropy in the northeastern Basin and Range where prior studies found prevalent depth-averaged positive radial anisotropy (Vsh > Vsv). This study focuses on depth-dependence of anisotropy and potentially distinct structures beneath three metamorphic core complexes (MCC's). Rayleigh and Love wave dispersion were measured using ambient noise interferometry and Bayesian Markov Chain Monte Carlo inversions for Vs structure were tested with several (an)isotropic parameterizations. Acceptable data fits with minimal introduction of anisotropy are achieved by models with anisotropy concentrated in the middle crust. The peak magnitude of anisotropy from the mean of the posterior distributions ranges from 3.5-5% and is concentrated at 8-20 km depth. Synthetic tests with one uniform layer of anisotropy best reproduce the regional mean results with 9% anisotropy at 6-22 km depth. Both magnitudes are feasible based on exhumed middle crustal rocks. The three MCC's exhibit ~5% higher isotropic upper crustal Vs, likely due to their anomalous levels of exhumation, but no distinctive (an)isotropic structures at deeper depths. Regionally pervasive middle crustal positive radial anisotropy is interpreted as a result of sub-horizontal foliation of mica-bearing rocks deformed near the top of the ductile deformation regime. Decreasing mica content with depth and more broadly distributed deformation at lower stress levels may explain diminished lower crustal anisotropy. Absence of distinctive deep crustal Vs beneath the MCC's suggests over-printing by ductile deformation since the middle Miocene.

A Middle Crustal Channel of Radial Anisotropy Beneath the Northeastern Basin and Range

Justin Wilgus[1], Chengxin Jiang[1*], Brandon Schmandt[1]
1. Department of Earth and Planetary Sciences, University of New Mexico, Albuquerque, NM, USA
*now at Research School of Earth Sciences, The Australian National University, Acton, ACT, Australia

Corresponding author: Justin Wilgus (jwilgus@unm.edu)

Key Points

- Evidence for a channel of positive radial anisotropy with peak magnitude at depths of ~8-20 km throughout the study area
- Absence of locally distinctive deep crustal V_S beneath core complexes suggests over-printing by middle Miocene regional ductile extension
- Diminished anisotropy in the hotter lowermost crust may result from decreased mica abundance and a transition to more distributed strain

Abstract

A challenge in interpreting the origins of seismic anisotropy in deformed continental crust is that composition and rheology vary with depth. We investigated anisotropy in the northeastern Basin and Range where prior studies found prevalent depth-averaged positive radial anisotropy (V_{SH} > V_{SV}). This study focuses on depth-dependence of anisotropy and potentially distinct structures beneath three metamorphic core complexes (MCC's). Rayleigh and Love wave dispersion were measured using ambient noise interferometry and Bayesian Markov Chain Monte Carlo inversions for V_S structure were tested with several (an)isotropic parameterizations. Acceptable data fits with minimal introduction of anisotropy are achieved by models with anisotropy concentrated in the middle crust. The peak magnitude of anisotropy from the mean of the posterior distributions ranges from 3.5-5% and is concentrated at 8-20 km depth. Synthetic tests with one uniform layer of anisotropy best reproduce the regional mean results with 9% anisotropy at 6-22 km depth. Both magnitudes are feasible based on exhumed middle crustal rocks. The three MCC's exhibit ~5% higher isotropic upper crustal V_S, likely due to their anomalous levels of exhumation, but no distinctive (an)isotropic structures at deeper depths. Regionally pervasive middle crustal positive radial anisotropy is interpreted as a result of sub-horizontal foliation of mica-bearing rocks deformed near the top of the ductile deformation regime. Decreasing mica content with depth and more broadly distributed deformation at lower stress levels may explain diminished lower crustal anisotropy. Absence of distinctive deep crustal V_S beneath the MCC's suggests over-printing by ductile deformation since the middle Miocene.

Plain Language Summary

The northeastern Basin and Range is an area of Earth's crust that has been dramatically stretched and thinned by tectonic forces. Seismic anisotropy, or wave speed dependence on direction, can provide useful insights into the way in which such deformation organizes crustal structure over long periods of time. We used surface waves to identify discrepancies between horizontally and vertically polarized wave speeds. Anisotropy focused in the middle crust at ~8-20 km is found to best resolve the observed discrepancies. The results suggest that development and preservation of anisotropy is more effective in the middle crust compared to the lowermost crust. The transition with depth may be explained by increasingly high temperature in the lowermost crust that reduces the abundance of highly anisotropy mica minerals and promotes ductile flow that is distributed across larger volumes rather than localized shear zones. Additionally, we find that areas of exceptionally localized extension called metamorphic core complexes have middle-to-lower crustal seismic structure that is similar to the surrounding region despite their distinctive upper crustal structure. These structures formed early in the development of the Basin and Range, consequently we suggest that subsequent ductile deformation in the middle-to-lower crust largely over-printed their structural legacies.

1. Introduction

The central-to-northern Basin and Range province of the western U.S. Cordillera is an area of large magnitude extensional strain, with up to ~100% regional-scale crustal extension since the Eocene (Hamilton and Myers, 1966; Wernicke et al., 1988; McQuarrie and Wernicke, 2005; Colgan and Henry, 2009; Long, 2018). Embedded within this region of distributed deformation are localized zones of more extreme extension and exhumation recorded in metamorphic core complexes (MCC), which expose rocks that were deformed below the brittle-ductile transition and exhumed during the development of the Basin and Range (e.g., Crittenden et al., 1980; Whitney et al., 2013; Platt et al., 2015). Regional-scale extensional strain rate peaked in the middle Miocene (McQuarrie and Wernicke, 2005; Colgan and Henry, 2009). Slower but ongoing right-lateral transtensional deformation is identified by geodetic studies, with ~1 cm/year northwest-directed relative motion between the low-strain crustal blocks of the Sierra Nevada and Colorado Plateau located on either side of the central-to-northern Basin and Range (Bennett et al., 2003; Hammond and Thatcher, 2004). As a result of the well-constrained deformation over geological and contemporary time scales, the Basin and Range and its internal MCC's are useful places to study potential indicators of how subsurface strain is organized, such as seismic anisotropy.

In this study, we investigate links between deformation recorded at the surface and the development of radial seismic anisotropy in extended continental crust. We focus on the northeastern Basin and Range surrounding three MCC's: the Ruby Mountains, Snake Range, and Albion-Raft River-Grouse Creek (Fig. 1). The distribution of crustal anisotropy is a subject of expanded investigation in recent years, in part due to the development of seismic noise interferometry methods that enable extraction of short-period surface wave measurements between pairs of seismographs (e.g., Shapiro and Campillo, 2004; Sabra et al., 2005). Inter-station noise interferometry is powerful for crustal imaging with dense and large aperture seismic arrays like the Transportable Array (TA) component of EarthScope's USArray, which provides excellent geographic distributions of short-period Rayleigh and Love wave paths compared to relying on earthquakes (e.g., Lin et al., 2008). This study focuses on radial anisotropy, which makes the simplifying assumption of transverse isotropy with a vertical symmetry axis to explain inconsistencies between Rayleigh and Love wave dispersion with independent horizontally and vertically polarized V_S, referred to as V_{SH} and V_{SV} (Babuska and Cara, 1991).

Prior investigation of radial anisotropy beneath the Basin and Range used TA data to find that positive radial anisotropy ($V_{SH} > V_{SV}$) is prevalent in the crust and correlated with areas of extensional deformation (Moschetti et al., 2010a,b). Crustal radial anisotropy has been detected in other parts of the North American Cordillera including the southern California transform margin (Wang et al., 2018), the Rio Grande rift (Fu and Li, 2015), the Canadian Rockies (Dalton and Gaherty, 2013), and Alaska (Feng and Ritzwoller, 2019). Globally, crustal radial anisotropy has been identified in many continental areas including tectonically active and cratonic settings (e.g., Shapiro et al., 2004; Sherrington et al., 2004; Huang et al., 2010; Duret et al., 2010; Xie et al., 2013; Luo et al., 2013; Cheng et al., 2013; Harmon and Rychert, 2015; Dreiling et al., 2018;

Ojo et al., 2017; Lynner et al., 2018). The most conventional interpretation for its origin is the strain-induced alignment of anisotropic crustal minerals forming an aggregate crystallographic preferred orientation (CPO; Mainprice and Nicolas, 1989; Weiss et al., 1999). However, there are plausible alternatives or additional contributions such as preferentially oriented fractures in the shallow crust, sedimentary stratigraphy, and organization of partial melt or fluids that may be prevalent in thick orogenic crust or magmatic systems (e.g., Leary et al., 1990; Backus, 1962; Hacker et al., 2014; Matharu et al., 2014; Almqvist and Mainprice, 2017; Harmon and Rychert, 2015; Jaxybulatov et al., 2014; Jiang et al., 2018; Lynner et al., 2018). The thin crust of the modern Basin and Range makes pervasive mid-crustal melting less likely compared to settings such as the Tibetan plateau, which has about double the thickness of radiogenic heat-producing crust (e.g., Hacker et al., 2014). Moschetti et al. (2010a) favor CPO as the most probable origin of radial anisotropy in the highly extended middle and lower crust of the Basin and Range, and laboratory measurements of exhumed rocks from the Basin and Range support the presence of CPO-derived anisotropy and the approximate validity of transverse isotropy (Erdman et al., 2013).

We further investigate radial anisotropy in the northeastern Basin and Range with combined analysis of Rayleigh and Love waves extracted from TA data and a denser regional array centered on the Ruby Mountains MCC (Fig. 1). Prior investigations using only the TA lacked the seismograph density to identify potentially anomalous anisotropy beneath Ruby Mountains MCC and focused on establishing the necessity of regionally prevalent anisotropy by assuming a uniform distribution in the middle and lower crust (Moschetti et al., 2010a). This study evaluates whether distinctive radial anisotropy exists beneath the Ruby Mountains or other MCC's in the northeastern Basin and Range. We also evaluate depth dependence of radial anisotropy to identify how depth-dependent composition and rheology may influence development of crustal radial anisotropy.

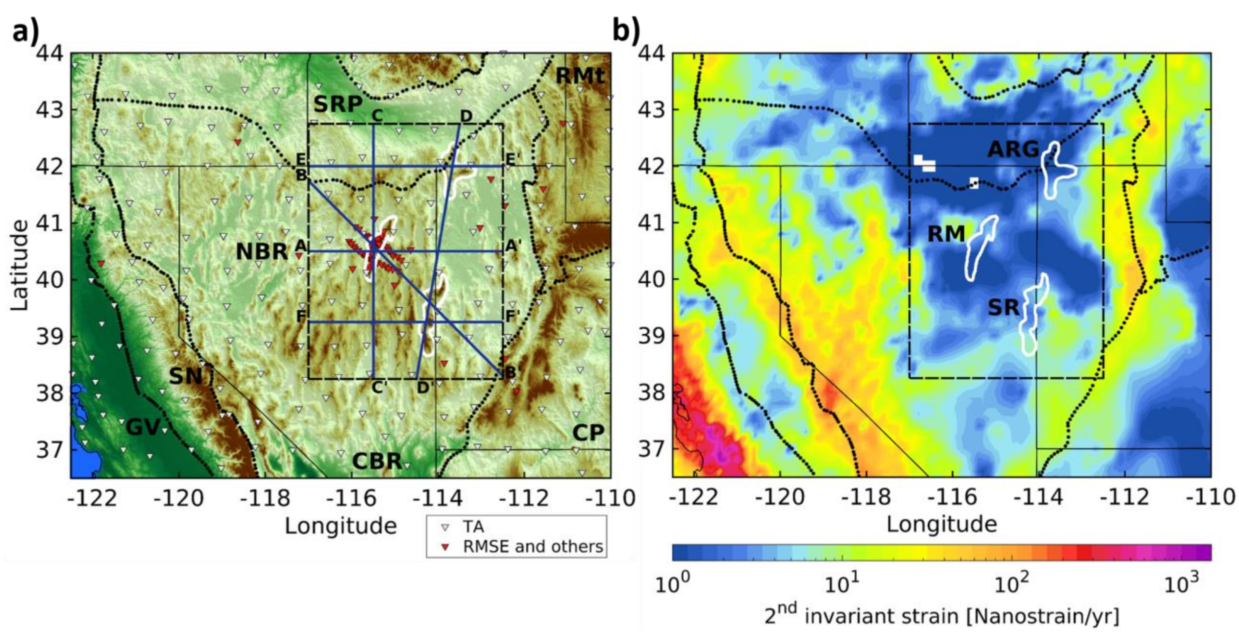

Figure 1. Maps of seismic data coverage and active regional deformation. (a) Broadband seismographs used for ambient noise cross correlations including the RMSE (red) and Transportable Array (TA) stations (white) used in the USANT model. Black dotted lines define geologic provinces from Fenneman, (1917): Colorado Plateau (CP), Great Valley (GV), northern Basin and Range (northern Basin and Range), central Basin and Range (CBR), Rocky Mountains (RMt), Sierra Nevada (SN), Snake River Plain (SRP). Black dashes delineate the focus area used in subsequent figures. Solid blue lines delineate surface trace of cross sections shown in Fig. 7. (b) Regional second invariant of strain rate estimated from inversion of GPS measurements (Kreemer et al., 2014). White outlines show metamorphic core complexes of the northern Basin and Range: Albion-Raft River-Grouse Creek (ARG), Ruby Mountains-East Humboldt (RM), Snake Range (SR).

2. Geologic and geodynamic setting

Formation of the Basin and Range as a province of extensional deformation and intraplate magmatism began in the Paleogene and closely followed cessation of Mesozoic crustal shortening that culminated with the Sevier and Laramide orogenies (Coney and Harms, 1984). Western plate boundary re-organization including subduction of the Kula-Farallon and Pacific-Farallon ridges decreased subduction zone width and coincided with the transition from dominantly compressional to extensional deformation in the Cordilleran interior (Schellart et al., 2010). Diminished compressional stress and thick elevated continental crust gave rise to gravitational collapse in what became the Basin and Range (Coney and Harms, 1984; Dewey, 1988; Rey et al., 2001). Post-orogenic collapse began with voluminous magmatism and localized extension sweeping from north to south in the Eocene and Oligocene, while regional scale extension dominantly occurred in the middle Miocene (Best and Christiansen, 1991; Wernicke and Snow, 1998; Colgan and Henry, 2009; Camp et al., 2015). Columbia River, Steens, and northern Nevada Rift basaltic volcanism (~15-17 Ma) were approximately coeval with Miocene acceleration of extension in the northern Basin and Range, suggesting that mantle upwelling further contributed to driving extensional collapse (Colgan and Henry, 2009; Camp et al., 2015). Continued growth of the San Andreas transform boundary since ~10 Ma was accompanied by an increasing component of right-lateral shear strain and concentration of strain near the boundaries of the Basin and Range compared to its interior (Wernicke and Snow, 1998; Colgan and Henry, 2009). Slow contemporary strain rates (Fig. 1; Bennett et al., 2003; Hammond and Thatcher, 2004; Kreemer et al., 2014) are consistent with minor amounts of slip on extensional faults in the north-central Basin and Range from the late Miocene through the Holocene (Pérouse and Wernicke, 2017).

Within the northern Basin and Range are three MCCs: the Ruby Mountains-East Humboldt Range, Snake Range, and Albion-Raft River-Grouse Creek Mountains (Fig. 1). This study benefits from data collected by the recent Ruby Mountains Seismic Experiment (RMSE), which provides exceptionally dense, ~5-10 km spacing, broadband seismograph coverage of the Ruby Mountains (Fig. 1; Litherland and Klemperer, 2017). The northern Ruby Mountains expose Proterozoic to Paleozoic metasedimentary rocks of the miogeocline that were intruded by Mesozoic to early Cenozoic plutons, buried during crustal shortening of the Sevier Orogeny, and then subjected to multiple phases of exhumation beginning in the late Cretaceous (Hodges et al., 1992; MacCready et al., 1997; Sullivan and Snoke, 2007). The southern Ruby Mountains expose unmetamorphosed Paleozoic sedimentary rocks that have not been buried below their stratigraphic depths (Colgan et al., 2010). Intrusion of the Harrison Pass pluton into the transition between the southern and northern Ruby Mountains occurred at ~36 Ma during an Eocene to Oligocene period of ductile shear deformation in the middle crust (Barnes et al., 2001; MacCready et al., 1997). Exhumation and extension in the southern Ruby Mountains were concentrated in the middle Miocene from ~17-10 Ma (Colgan et al., 2010; Haines and van der Pluijm, 2010).

The Snake Range and Albion-Raft River-Grouse Creek (ARG) MCCs are included in the study area, but data coverage in these regions are mainly provided by the TA seismographs spaced ~70 km apart (Fig. 1, Supplementary Information S1, T1). The Snake Range MCC exposes Proterozoic to Cenozoic strata and records up to ~450% extension of the brittle upper crust (Lee et al., 1987). Metamorphism and ductile deformation of the deeply exhumed footwall dominantly occurred from the Oligocene to early Miocene, ~35-20 Ma, followed by fault-driven exhumation to within ~3 km of the surface in the middle Miocene, ~17 Ma (Miller et al., 1999; Gébelin et al., 2011). In the ARG, outcrops expose Archean to Cenozoic stratigraphic units (Compton et al., 1977), and metamorphism of gneiss domes there dominantly occurred in the Oligocene, ~34-25 Ma (Egger et al., 2003; Konstantinou et al., 2013). The ARG exposes strata exhumed from ~10 km greater depth than in the surrounding region, however much of the exhumation was likely driven by locally pronounced thermal weakening of the crust and ascent of granitic diapirs during the Oligocene (Konstantinou et al., 2013). A later phase of fault-driven Miocene exhumation from ~15-7 Ma led to the surface exposures of the ARG MCC (Wells et al., 2000; Egger et al., 2003).

Modern lithospheric structure of the northern Basin and Range is characterized by high heat flow, thin continental mantle lithosphere, and a low-relief Moho interface defining an average crustal thickness of ~30-35 km (Hasterok and Chapman, 2007; Klemperer et al., 1986; Zandt et al., 1995; Lowry and Pérez-Gussinyé, 2011; Gilbert et al., 2012; Schmandt et al., 2015). Contemporary heat flow in the northern Basin and Range has an estimated median of 79 mW/m^2, which is consistent with steady-state thermal lithospheric thickness of ~75 km (Hasterok and Chapman, 2007). Teleseismic imaging with P-to-S and S-to-P converted waves indicates a sharp lithosphere-asthenosphere boundary at similar or shallower depths of ~55-75 km, and the sharpness and amplitude of the interface, along with temperature estimates from seismic tomography, suggest it may be defined by partial melt at the base of the lithosphere (Levander and Miller, 2012; Lekić and Fischer, 2014; Hansen et al., 2015). Controlled source seismic reflection studies show steeply dipping normal faults in the upper crust, $\lesssim$6-8 km, transitioning to prevalent sub-horizontal layering in the middle and lower crust underlain by lower reflectivity mantle lithosphere (e.g., Klemperer et al., 1986; McCarthy, 1986; Hauser et al., 1987; Holbrook et al., 1991; Stoerzel and Smithson, 1998). Fine-scale deep crustal layering illuminated by high frequency reflections may be due to a combination of ductile extension accommodated by localized shear zones and intrusion of mafic sills during the late Eocene through Miocene magmatic flare-up in the Basin and Range (Klemperer et al., 1986; Gans, 1987; McCarthy and

Thompson, 1988; Valasek et al., 1989; Holbrook et al., 1991). Regional ductile flow in the middle-to-lower crust during and after the middle Miocene phase of regional extension is likely based on the low-relief Moho surface, estimated modern Moho temperatures of ~600-800 °C, and decoupling of azimuthal anisotropy in the crust and mantle (Klemperer et al., 1986; Gans, 1987; Block and Royden, 1990; Schutt et al., 2018; Lin et al., 2011).

3. Data and Methods

3.1 Data

Continuous three-component (3-C) broadband seismic data were collected from the RMSE (Litherland and Klemperer, 2017) and surrounding permanent network stations (Fig. 1; Supplementary Information T1). Using inter-station measurements of surface wave propagation extracted from empirical Green’s functions estimated using ambient noise interferometry we obtain Rayleigh and Love wave data (Fig. 2; Bensen et al., 2007). Prior to the RMSE the TA, deployed from ~2006–2008, provided the best broadband coverage of the study area in the northern Basin and Range with ~70 km spacing. The RMSE deployed 50 3-C broadband seismometers ~5–10 km apart along three transects across the Ruby Mountains between 2010–2012, thereby providing opportunities for improved resolution of regional crustal structure.

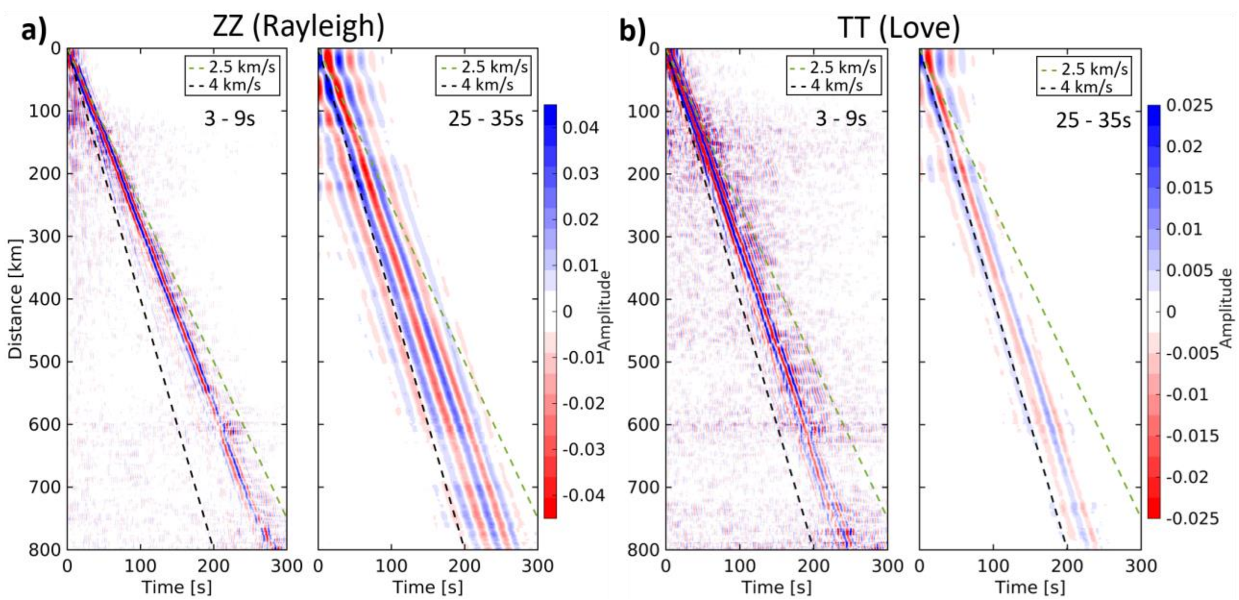

Figure 2. Stacked noise correlations from the RMSE and regional seismographs. (a) Stacked time versus distance image of 3260 vertical component (ZZ) inter-station noise cross correlations recorded over ~18 months for the RMSE and exterior stations (red triangles in Figure 1). Correlations bandpass filtered between 3-9 s and 25-35 s period are shown in the left and right panels, respectively. Longer periods propagate at higher velocities as expected for dispersive Rayleigh waves. (b) same as (a), but TT component correlations are plotted to show Love waves.

3.2 Phase velocities

Inter-station Rayleigh and Love wave dispersion measurements from two different time periods were used to invert for radially anisotropic V_S structure. Rayleigh and Love wave dispersion measurements were made with the vertical (ZZ) and transverse (TT) noise cross-correlation functions, respectively (Fig. 2). Inter-station dispersion measurements from Ekström, (2017) were used for the TA time period 2005-2008. New noise cross-correlations functions were calculated for the RMSE deployment from 2010-2012 (Fig. 2). To better merge the RMSE and TA time period measurements, inter-station noise cross-correlation functions were calculated for the RMSE and a set of 26 azimuthally distributed permanent seismographs operating between 2010-2012 (Fig. 1 and Supplementary Information S1). We followed Bensen et al., (2007) to process the new noise cross-correlation measurements, with the slight modification of using half-overlapping 4-hour, rather than daily, time windows (e.g., Seats et al., 2012). Rayleigh and Love wave phase velocities were estimated at 5-30 s periods using frequency-time analysis (Bensen et al., 2007; Lin et al., 2008). Phase velocities from Ekström, (2017) were calculated using Aki's spectral formulation (Ekström et al., 2009), which produces results that are consistent with frequency-time analysis (Tsai and Moschetti, 2010). Three types of quality control were applied to the new dispersion measurements to ensure that: Rayleigh or Love wave signal-to-noise ratio is >6, phase velocity is between 2-5 km/s, and the inter-station distance is >2 wavelengths. Inter-station phase velocities were inverted for phase velocity maps for periods at 5-30 s for Rayleigh waves and 6-30 s for Love waves using a damped least-squares inversion and great circle ray paths following Ekström, (2017). RMSE measurements with misfits beyond 2 standard deviations were removed and the inversion was repeated once more (Supplementary Information S2).

3.3 Anisotropic V_S inversion

Models of V_S structure as a function of depth were estimated at each geographic location using a Bayesian Markov chain Monte Carlo (BMMC) inversion (Shen et al., 2012). Each V_S model is parameterized by a set of spline functions in the crust and a single layer in the upper mantle, and the number of splines in the crust and the assumption of isotropy or radial anisotropy were varied in different inversion cases described below (Fig. 3; Supplementary Information S3). Uniform prior distributions were assumed for the values of the spline coefficients. The range of V_S models permitted by the prior distribution is shown in Figure 3. Forward calculations of Rayleigh and Love dispersion curves were performed using the Computer Programs in Seismology software package (Herrmann, 2013). V_P and density needed for forward modelling were derived from the empirical scaling relationships of Brocher, (2005) for the crust. In the upper mantle, we use relative scalings from Panning & Romanowicz, (2006) based on the PREM model. Goodness of fit between predicted and observed dispersion curves was calculated with a standard chi-squared (χ^2) misfit, $\chi^2 = \sum((\text{obs - pred})^2/\sigma^2)$, using phase velocity uncertainties, σ, (Supplementary Information T2) from Jiang et al., (2018). Each 1D inversion was run for 1.5 million iterations and model selection is guided by the Metropolis - Hastings algorithm (Hastings, 1970;

Mosegaard and Tarantola, 1995). Because the χ^2 values of the best models vary spatially within the study area, the best 800 models are chosen to represent the posterior distribution. The mean of the posterior distribution at each geographic point is shown as the final result on a regular 0.25° grid.

To validate the necessity of seismic anisotropy in the crust and test the depth-dependence of radial anisotropy we constructed five different BMMC inversion parameterizations (Fig. 4). The five cases are: 1) isotropic crust (4 splines) and mantle; 2) isotropic crust (4 splines), anisotropic mantle; 3) isotropic crust (8 splines), anisotropic mantle; 4) anisotropic crust (4 splines), anisotropic mantle; 5) anisotropic middle crust (middle 2 of 4 splines), anisotropic mantle (Figs. 3 and 4). In each case the upper mantle layer extends to 100 km depth. PREM Vp/Vs and density are assumed at depths greater than the local Moho (Dziewonski and Anderson, 1981). Given the maximum period of 30 s used in this study, there is negligible sensitivity to structure at >100 km depth. V_{SH} and V_{SV} are independent in inversion cases that consider anisotropy. The resulting isotropic V_S models were estimated using Voigt averaging, $V_S = \sqrt{(2V_{SV}^2 + V_{SH}^2) / 3}$ and radial anisotropy was calculated post-inversion where, radial anisotropy = $100(V_{SH} - V_{SV})/ V_S$.

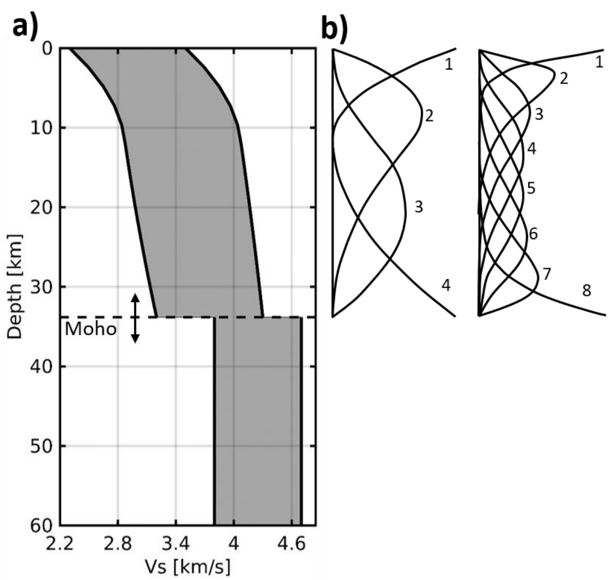

Figure 3. Prior model space range and b-spline parameterization of crustal V_S. (a) The range of V_S spanned by the prior distribution is shaded in the grey corridor. The example is shown with the regional mean Moho depth. (b) Parameterizations with 4 or 8 b-splines, which allow smoothly varying crustal V_S with a modest number of parameters compared to using discrete layers. In the different parameterization cases described in section 3.3 some, all, or none of the b-splines in the crust are allowed to be radially anisotropic.

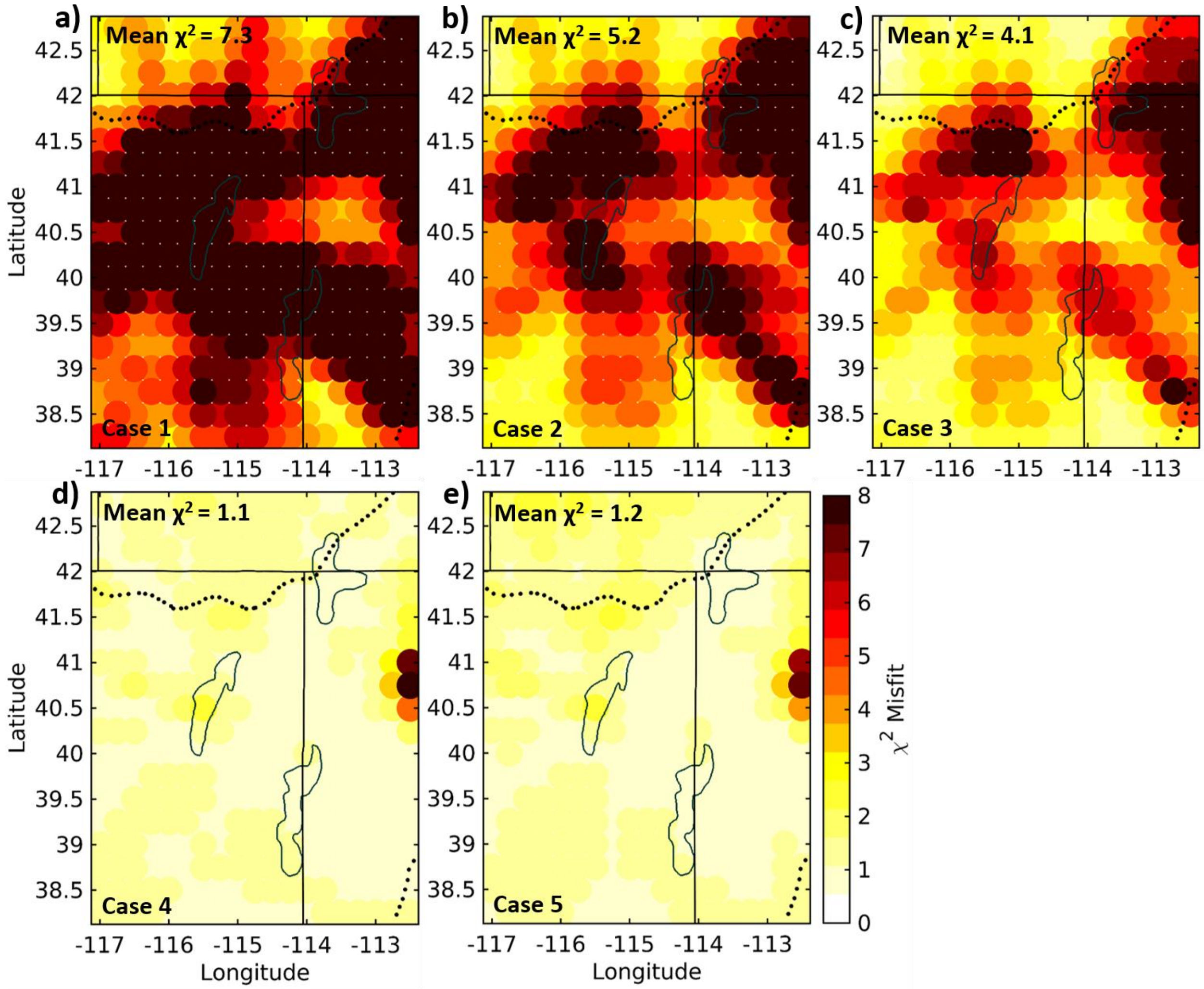

Figure 4. Data misfit maps for different inversion parameterizations. a-e) Chi-squared (χ^2) misfit maps for the five parameterization cases described in section 3.3. All maps correspond to inversions using the crustal thickness model of Schmandt et al., (2015). Regional mean χ^2 misfits are given in the upper left portion of each map. Maps in a-c correspond to inversions assuming isotropic V_S in the crust and exhibit high χ^2 misfits. Maps in d & e allow anisotropy in the entire crust and middle crust, respectively, and achieve similarly low regional mean χ^2 misfits.

Each of the five inversion parameterization cases were run using three different regional crustal thickness models (Fig. 5; Schmandt et al., 2015; Buehler and Shearer, 2017; Shen and Ritzwoller, 2016), and an interpreted local crustal thickness model calculated below each station within the RMSE (Fig. 5; Litherland and Klemperer, 2017). The motivation for testing the different crustal thickness models is to determine if the strength and pattern of radial anisotropy are dependent on the choice of crust thickness model. Only subtle variations were found in the radially anisotropic structure as a result of different crustal thickness models (Fig. 5; Supplementary Information S4 and S5). So, we primarily present results using the crust thickness model of Schmandt et al., (2015) which contains measurements from both RMSE and TA data.

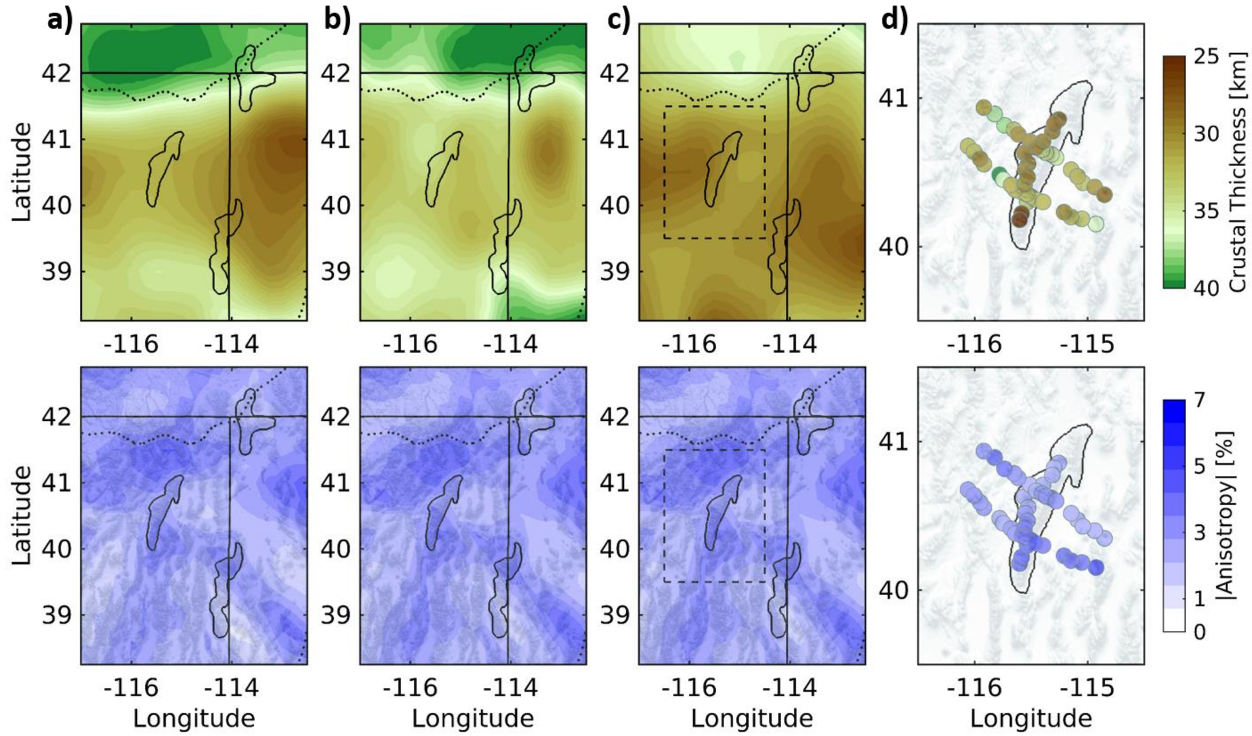

Figure 5. Effects of crust thickness models on estimates of crustal radial anisotropy. a) The top panel shows the crust thickness model of Schmandt et al., (2015) and the bottom panel shows the depth-integrated absolute value of radial anisotropy from inversion cases 4 in which anisotropy is allowed in all 4 crustal b-splines. b,c) Similar to (a) but showing results using the crustal thickness models of Buehler and Shearer, (2017) and (c) Shen and Ritzwoller, (2016), respectively. (d) Similar to a-c except local crustal thickness results from Litherland and Klemperer, (2017) are only available beneath stations from the RMSE array. Dashed lines in (c) demarcate the area shown in (d). Distribution and magnitude of anisotropy are similar regardless of the choice of crust thickness model.

4. Results

4.1 Regional mean misfit and radial anisotropy

The five model parameterization cases provide insight into the importance of crustal radial anisotropy and its depth dependence. Assuming isotropy in the crust (cases 1-3) results in large regional mean χ^2 misfits of ~4-7 (Fig. 4). Compared to the fully isotropic crust and mantle in case 1, parametrization allowing upper mantle radial anisotropy (case 2), reduces the regional mean χ^2 misfit from 7.3 to 5.2. Case 3 explores whether doubling the isotropic parameters in the crust can explain the Rayleigh-Love discrepancy without introducing crustal anisotropy. This approach with 8 isotropic b-splines slightly reduces the regional mean χ^2 misfit from 5.2 to 4.1. Introduction of radial anisotropy throughout the crust (case 4) and anisotropy focused in the middle crust (case 5) result in superior regional mean χ^2 misfits of ~1 (Fig. 4; Supplementary Information S4). Persistently high mean χ^2 misfits located on the eastern edge of the study region are coincident with, and likely influenced by, the deep (~3 km in this location) Great Salt Lake basin structure (Mikulich and Smith, 1974).

To further evaluate the depth dependence of radial anisotropy, additional tests were performed allowing the mantle and only a single crustal b-spline to be radially anisotropic in each test. Individually introducing radial anisotropy for either b-spline 2 or 3 also achieves low regional mean χ^2 misfits of 1.2 and 1.3, respectively (Fig. 6). Higher mean misfits of 2 and 3.3 were found when radial anisotropy was only allowed for b-spline 1 and 4, respectively. In these cases of only allowing radial anisotropy for the uppermost or lowermost b-spline, larger peak amplitudes of anisotropy were required, up to ~10-15%. Thus, crustal radial anisotropy is necessary to adequately fit the Rayleigh and Love wave dispersion measurements and it is possible to achieve similarly good fit to the data using only middle crustal radial anisotropy with a peak magnitude of ~4-5%. Prior studies show that assuming uniform radial anisotropy through the entire crust or confining it to the middle and lower crust, are alternative parameterization approaches that can achieve regional mean χ^2 misfits of ~1 (e.g., Xie et al., 2015; Moschetti et al., 2010a; Supplementary Information S6). These approaches are attractive for only requiring one anisotropic parameter, however the tests conducted here demonstrate that just one anisotropic parameter is equally effective if it is isolated to middle crustal depths (Fig. 6; Supplementary Information S6).

The depth of the regional mean peak radial anisotropy varies from 8-20 km for the parameterizations tested here that achieve regional mean χ^2 misfits of ~1. The shallowest peak and smallest magnitude, 8 km & 3.5%, is found if only b-spline 2 is anisotropic. The deepest peak depth and larger magnitude, 20 km & 5%, are found if only b-spline 3 is anisotropic. Among parameterizations allowing multiple anisotropic b-splines the peak depth and magnitude are 11 km & 5%, respectively, if all 4 b-splines are anisotropic (case 4) and 14 km & 3.5% if just b-splines 2 & 3 are anisotropic (case 5). The larger peak magnitude that occurs when all 4 b-splines are anisotropic is related to the introduction of negative anisotropy in much of the regional the upper crust and more sporadically in the lower crust.

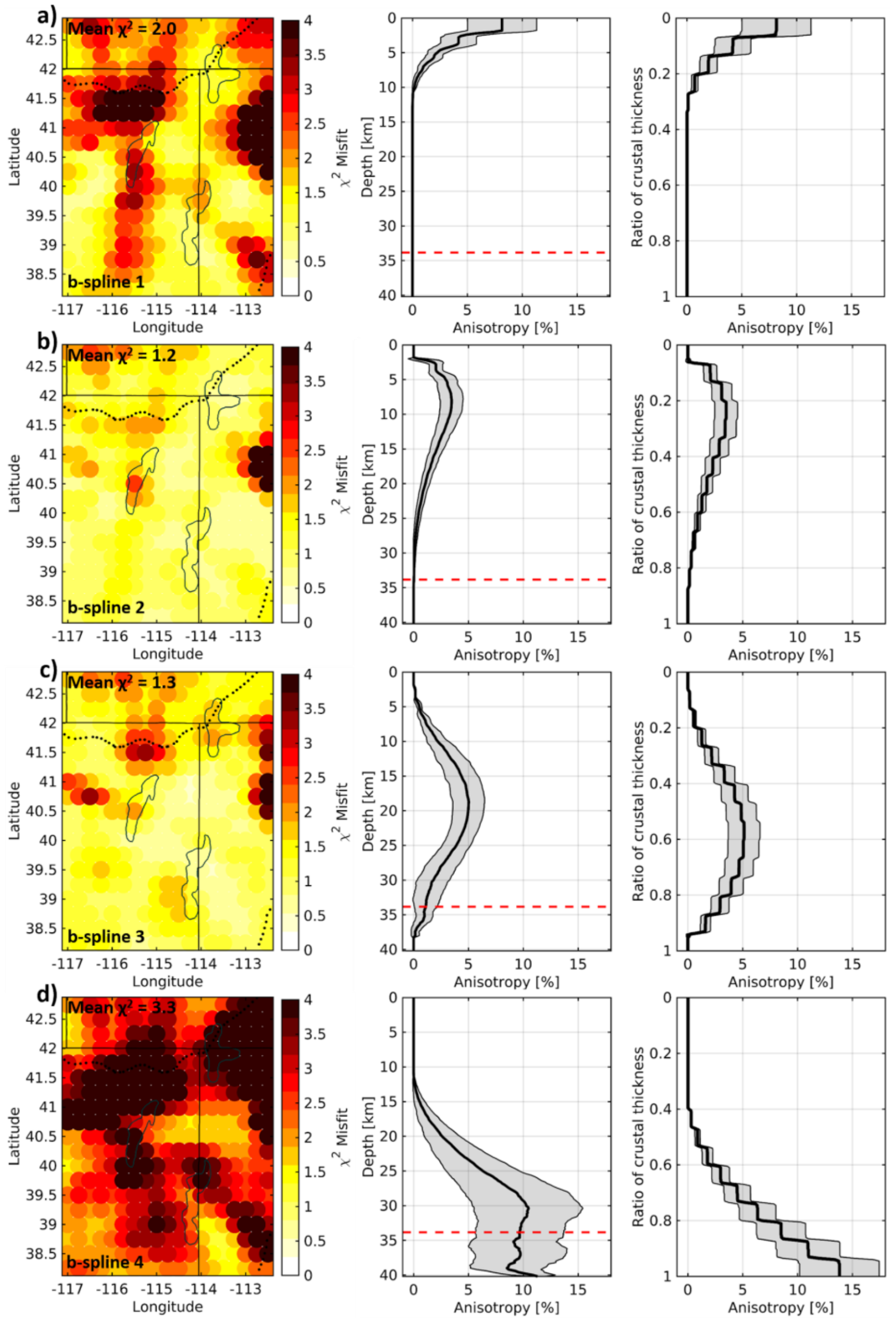

Figure 6. Misfit maps and anisotropic depth profiles for tests with anisotropy in one isolated crustal b-spline. a) Left panel shows the regional mean χ^2 misfit map if anisotropy is only allowed for b-spline 1. The crustal b-spline that is allowed to be anisotropic is labeled in the lower left corner of the map and the regional mean χ^2 misfit is labeled in the upper left corner of the map. Middle panel shows the resulting radial anisotropy profile including the mean (black line) and 1 standard deviation corridor (grey) of the posterior distribution. Right panel also shows the radial anisotropy depth profile but with depth normalized to local crustal thickness. All results shown in this figure correspond to inversions assuming the regional crust thickness model of Schmandt et al., (2015). Regional mean χ^2 misfits are given in the upper left portion of each map. b-d) Similar to as but showing results for tests allowing anisotropy individually in b-splines 2-4, respectively. Note that individually allowing radial anisotropy for b-splines 2 and 3 fits the data better than for splines 1 and 4, while requiring smaller magnitudes of anisotropy.

4.2 Variations in isotropic and anisotropic structure

Considering the broad depth sensitivity of surface waves we discuss the main results at 4 depth ranges: upper crust, middle crust, lower crust, and upper mantle (Fig. 7). The upper crust is set to extend from 0 - 5 km, where the first b-spline depth range dominates and the shortest period phase velocities in the inversion (6 s) have concentrated sensitivity. The depth extents of the middle and lower crust are determined by evenly splitting the remaining crust thickness. Since the major patterns in isotropic V_S variations remained consistent through the different radial anisotropy parameterization cases (Supplementary Information S7), we focus on describing inversion results from case 4 in which radial anisotropy was allowed at all crustal and upper mantle depths. The plotted results represent the mean isotropic V_S and anisotropy of the posterior distribution from the BMMC inversions for the region. To help identify where anisotropy may not be necessary to provide a similarly good fit to the data we also provide plots that show only areas where the absolute value of radial anisotropy has a statistical significance greater than one standard deviation of the posterior distribution (Fig. 7, 8; Supplementary Information S7 and S8-S10). In the upper crust negative radial anisotropy is more commonly observed than positive radial anisotropy, and in many areas its significance exceeds one standard deviation of the posterior distribution. The prevalence of upper crustal negative radial anisotropy is consistent with some prior studies suggesting the presence of vertical to sub-vertical cracks at low confining pressures (e.g., Crampin, 1994; Xie et al., 2013; Xie et al., 2017; Shirzad and Shomali, 2014). The middle crust shows only positive radial anisotropy and its significance is characteristically greater than one standard deviation of the posterior. In contrast, the lower crust shows areas of negative anisotropy but the significance of these measurements is typically smaller than one standard deviation of the posterior (Fig. 7).

Distinctive V_S structure beneath the three MCC's is identified for isotropic V_S in the upper crust, but the MCC's do not appear distinctive in radial anisotropy or middle-to-lower crustal isotropic V_S (Fig. 7 & Fig. 8). At upper crustal depths the three MCC's exhibit isotropic V_S that is ~5-7% higher than the regional mean (Fig. 7). In the middle crust the most prominent isotropic V_S features are relatively high V_S (+3-5%) beneath the Snake River Plain and relatively low V_S (-2 to -4%) in a ~west-east trending corridor that crosses the Ruby Mountains MCC but extends across the study area (Fig. 7). In a North-South cross-section the low V_S in the middle crust is co-located with the Ruby Mountains MCC (Fig. 8), but the map views show this is a larger feature almost orthogonal to the strike of the Ruby Mountains (Fig. 7). In the lower crust, the Snake River Plain is underlain by relatively high V_S (+4-6%) that extends southward across the physiographic boundary with the Basin and Range (Fig. 7). At upper mantle depths the highest V_S is found in the southwest portion of the study area toward the center of the Basin and Range, and the lowest V_S is found near the northwestern edge of the Colorado Plateau (Fig. 7). The patterns of isotropic V_S variations in the crust are consistent with prior tomography studies using TA data (e.g., Moschetti et al., 2010a,b; Schmandt et al., 2015; Shen and Ritzwoller, 2016). Radial anisotropy cross-sections highlight the widespread positive radial anisotropy (+3-5%) that forms a channel at middle crustal depths (Fig. 8). In general, the magnitude and depth of radial anisotropy do not abruptly change near the MCC's. However, there is one notable local disruption of the middle crustal positive radial anisotropy channel near the Snake Range MCC (Fig. 8d,f).

Perhaps the most important new result from this study is the evidence suggesting depth-dependent radial anisotropy in the form of a regional middle-crustal channel of positive radial anisotropy (~3-5%). From a reductionist perspective it is informative that the parameterization tests show the Rayleigh-Love discrepancy can be adequately resolved by only introducing positive radial anisotropy in the middle crust (b-splines 2 and/or 3). Additionally, a peak magnitude of radial anisotropy of ~4% is sufficient if radial anisotropy is restricted to b-spline 2 or depths of ~5-15 km, whereas greater magnitudes of up to 10-15% are needed to explain the Rayleigh-Love discrepancy if radial anisotropy is only allowed deeper or shallower (Fig. 6).

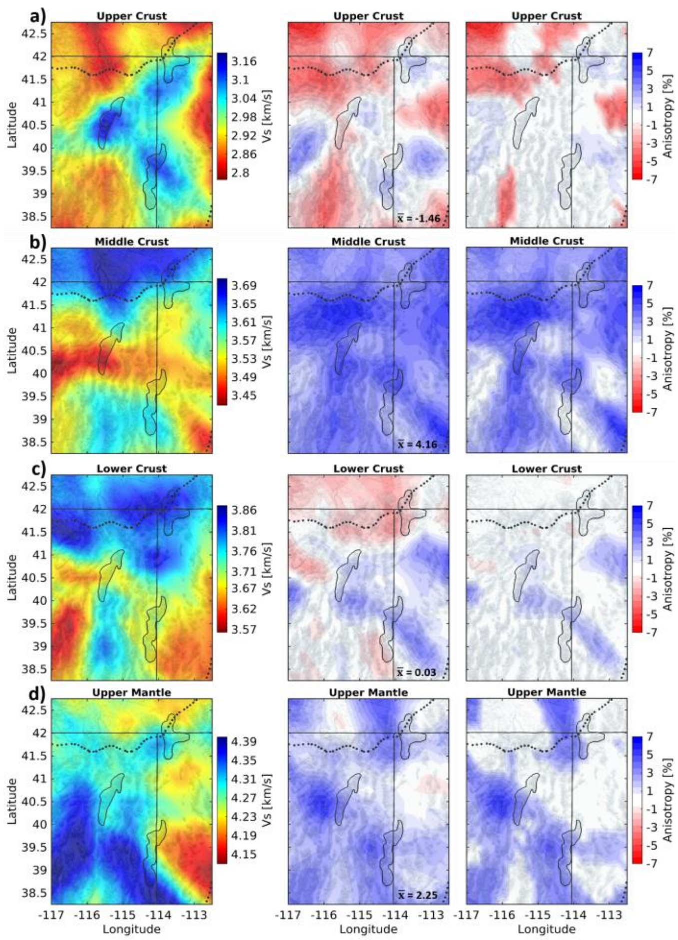

Figure 7. Depth averaged isotropic V_S and radial anisotropy maps for the upper crust, middle crust, lower crust, and upper mantle. (a) Depth averaged isotropic V_S and radial anisotropy of the upper crust. Left panel shows isotropic velocity. Middle panel shows radial anisotropy results. The depth averaged mean radial anisotropy of the map area ($\bar{\mathbf{x}}$) is given in the lower right corner. Right panel shows only results that have an absolute value of radial anisotropy with a statistical significance greater than one standard deviation of the posterior distribution. The upper crust maps average results between 0 and 5 km while the extent of depth averaging of the middle and lower crust is determined by evenly splitting the remaining thickness between 5 km and the Moho at each inversion point. (b-d) Same as (a) but for the middle and lower crust and upper mantle, respectively. All results shown in this figure are from inversion case 4 and correspond to inversions assuming the regional crust thickness model of Schmandt et al., (2015).

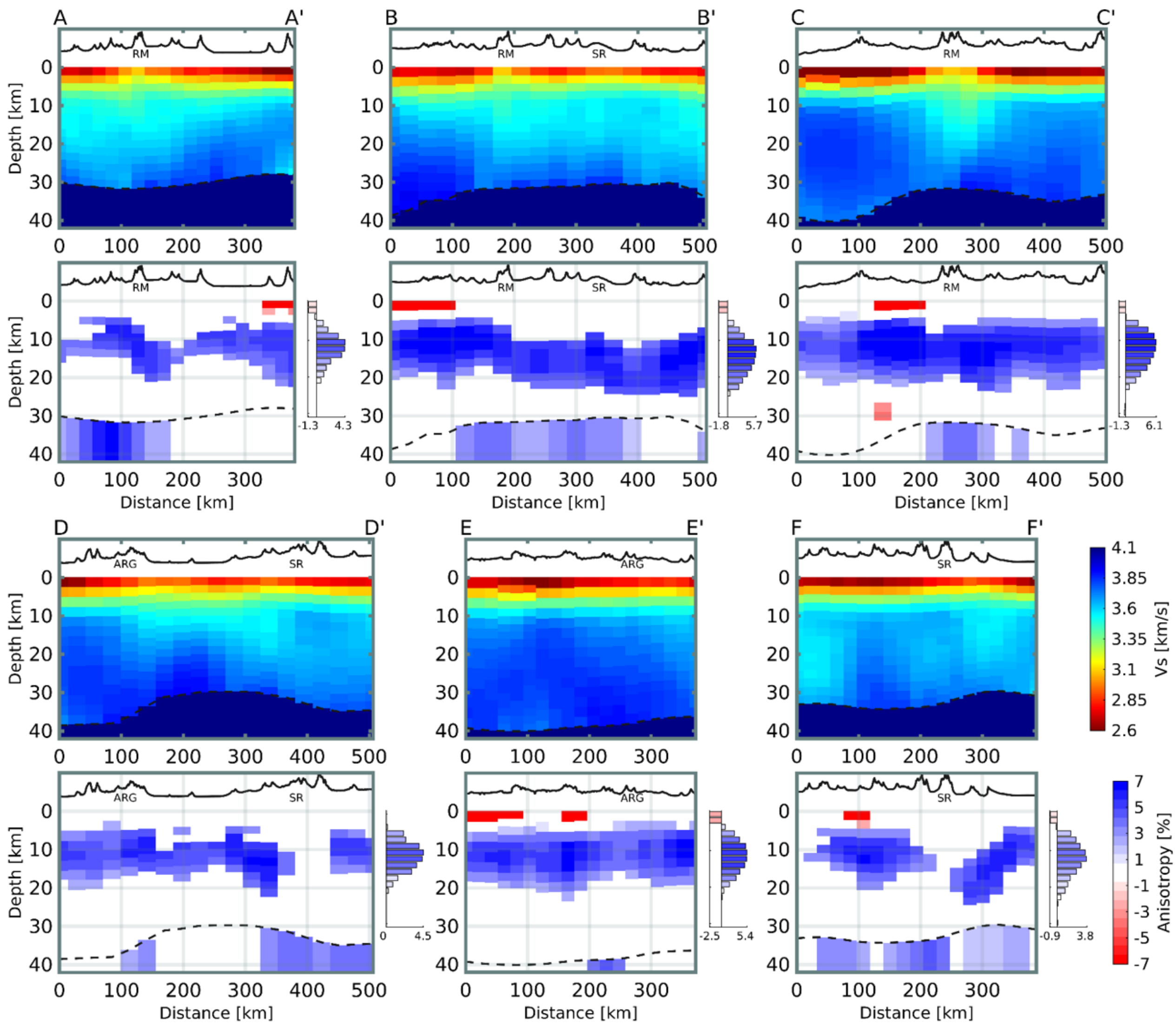

Figure 8. Cross sections (see figure 1) showing isotropic V_S and anisotropy results from inversion case 4 using the crustal thickness (dashed line) model of Schmandt et al., (2015). Bar charts right of anisotropy cross sections show average anisotropy profiles with depth for each cross section. Anisotropy minima and maxima are labeled on the x axis of each profile and colors correspond to anisotropy color bar. The radial anisotropy cross-sections (lower panels) in a-f show only results that have an absolute value of radial anisotropy with a statistical significance greater than one standard deviation of the posterior distribution. Topography is exaggerated 3 times in the profiles at the top of each panel.

4.3 Synthetic resolution tests

Resolution tests using synthetic dispersion curves generated from known V_S models confirm that a middle crustal channel of radial anisotropy is resolvable and provide insight into the optimal depth range and magnitude of anisotropy for matching the observational results. The synthetic V_S model posterior that best matches the regional mean structures includes 9% radial anisotropy from 6-22 km depth and 5% radial anisotropy in the upper mantle (Fig. 9a). A test with 9% radial anisotropy extending from 6 km to the Moho does not match the diminishing radial anisotropy with depth found in the inversion results based on observational data (Fig. 9b). A test with weaker lower crustal radial anisotropy of 4% is also consistent with the regional mean from the observational results (Fig. 9c). Therefore, although the magnitude of anisotropy in the lower crust is not as strong as it is in the middle crust, the dispersion data cannot discriminate whether lower crustal radial anisotropy is somewhat weaker than that of the middle crust or absent entirely.

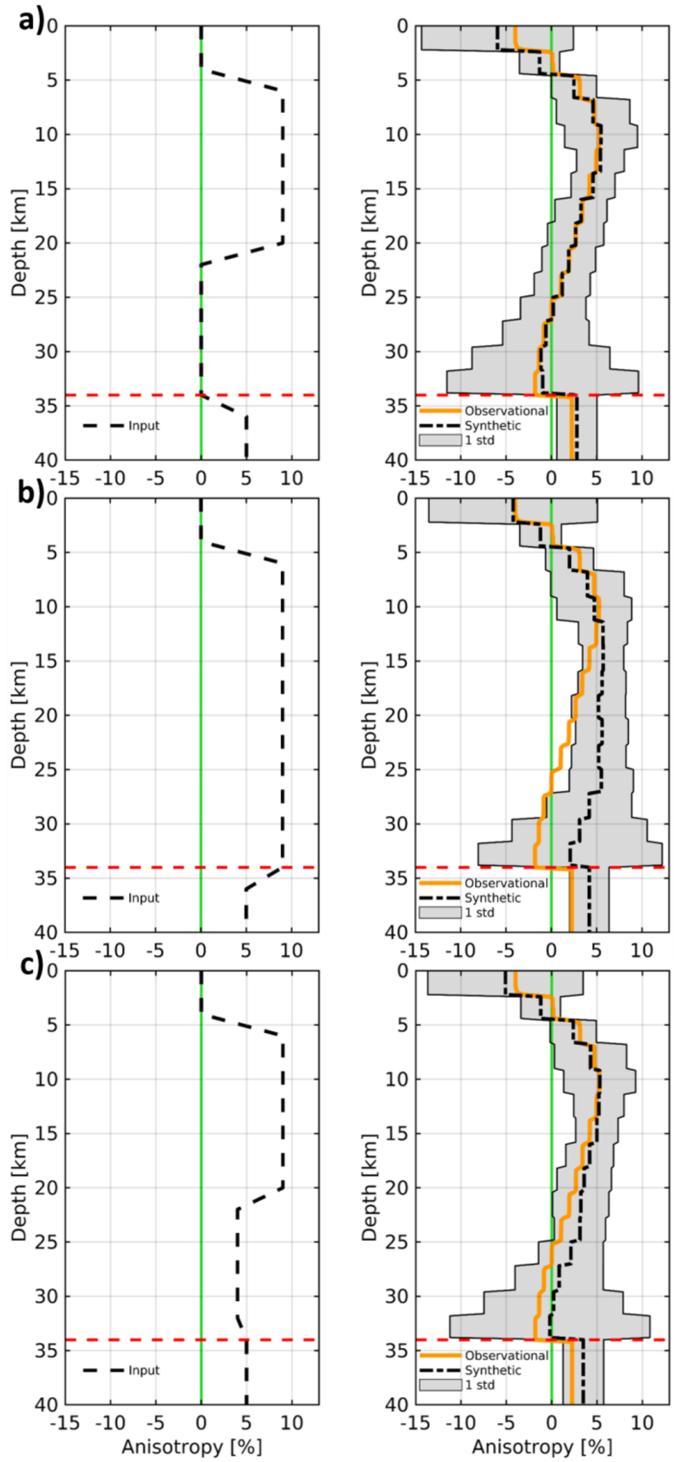

Figure 9. Synthetic resolution tests. (a) Left panel shows resolution test input (dashed line) of 9% radial anisotropy from 6-22 km and 5% in the upper mantle. Right panel shows resulting mean radial anisotropy model (dash-dotted line) from the forward calculation and one sigma corridor (shaded gray region) of the modeled posterior distribution. Dark green line shows observed mean model from inversion case 4. (b) Same as (a) but with 9% radial anisotropy throughout the crust as input. (c) Same as (b) but with 4% radial anisotropy in the lower crust, 22 km to 34 km.

4.4 Uncertainties due to modeling assumptions

Perhaps the most important source of uncertainty in the results lies in the validity of the radial anisotropy assumption. In this study, transverse isotropy (referred to as hexagonal symmetry in crystallography) with a vertical symmetry axis is assumed. This assumption is approximately valid for many deformed crustal rock samples (Erdman et al., 2013; Brownlee et al., 2017) and is common in studies seeking to explore seismic anisotropy via the Rayleigh-Love discrepancy. In some studies, this is also referred to as 'apparent radial anisotropy' (e.g., Xie et al., 2015; Xie et al., 2017, Feng et al., 2019). However, different forms of anisotropy and spatial variations in the tilt of the symmetry axis are likely to be present based on common crustal lithologies (Tatham et al., 2008; Ward et al., 2012; Erdman et al., 2013; Brownlee et al., 2017; Almqvist and Mainprice, 2017). Allowing for more complex forms of anisotropy, such as an oriented hexagonal or orthorhombic tensor would come with the tradeoff of estimating a greater number of model parameters, and prior results find that our study area is relatively well-suited to the simpler assumption of transverse isotropy. Xie et al., (2015) inverted surface wave dispersion and ellipticity measurements allowing for hexagonal anisotropy with a spatially variable tilt axis, and found that dip angles of the symmetry axis are relatively small, ~15-25°, in the northeastern Basin and range compared to the western U.S. average, ~25-30°. This would cause our estimates of radial anisotropy to be slight underestimates compared to the oriented elastic tensor approach of Xie et al., (2015). The simpler approach adopted here allows for efficient testing of several parameterizations that provide new insights into the depth dependence of radial anisotropy.

Another source of modeling uncertainty is the assumption of an empirical V_P/V_S scaling (Brocher, 2005), which could bias the radial anisotropy results especially in cases of strongly anomalous V_P/V_S that might be associated with deep sedimentary basins or the alpha-beta quartz transition in thick continental crust (Gao and Lekić, 2018). In the absence of strong constraints on V_P across the study area we consider the empirical V_P/V_S scaling relationship a reasonable assumption. Future studies incorporating additional measurements such as Rayleigh wave ellipticity (e.g., Lin et al., 2014; Gao and Lekić, 2018) and P wave reflectivity from ambient noise or coda autocorrelation (e.g., Gorbatov et al., 2012; Tibuleac and von Seggern, 2012; Delph et al., 2019) offer opportunities to better mitigate tradeoffs between V_P/V_S and crustal radial anisotropy.

5. Discussion

5.1 Upper Mantle

The surface wave period range used here (5-30s) is most sensitive to crustal structure, but due to tradeoffs between lower crust and upper mantle structure it is worth noting that the isotropic and anisotropic upper mantle results from this study are consistent with previous studies incorporating longer period measurements. Relatively high isotropic V_S , ~4.3-4.4 km/s, in the uppermost mantle of the southwest portion of the study region agrees with prior V_S tomography incorporating longer period surface waves and receiver functions (Shen and Ritzwoller, 2016) and appears to be correlated with positive radial anisotropy in the same region (Fig. 7). The results presented here also confirm that positive radial anisotropy of ~2-5% is widespread in the uppermost mantle beneath the Basin and Range as found by recent long period waveform tomography (Yuan et al., 2014; Zhu et al., 2017; Clouzet et al., 2018).

5.2 Links between MCC's and V_S structure

The anomalous degree of exhumation and extension evident at the surface in MCC's motivates inquiry into how MCC formation is manifested in sub-surface V_S structure. The three MCC's in the study area are closely correlated with relatively high V_S, + 4-7%, in the upper crust (Fig. 7). Continental crustal V_S generally increases with depth (Christiansen and Mooney, 1995; Laske et al., 2013: Tesauro et al., 2014; Shen et al, 2016) and in these locations crustal rocks have been exhumed from the middle-to-lower crust to the surface. We therefore interpret these relatively high V_S regions to be a simple consequence of the locally anomalous exhumation (Fig. 7a). Comparison of the average V_S structure beneath the three MCC's with the average across the study area further shows the distinctly higher V_S in the upper crust (Fig. 10). In contrast, middle-to-lower crustal V_S and radial anisotropy depth profiles averaged beneath the three MCC's are strikingly similar to those averaged across the study area (Fig. 10). This similarity suggests that either MCC formation had little effect on deep crustal structure (V_S and anisotropy) or that the effect of MCC formation on deep crustal structure has been overprinted.

Models of MCC formation, particularly for rapidly exhumed MCC's, predict locally sub-vertical flow lines associated with anomalous levels of exhumation and partial melting of the middle crust (Rey et al., 2009a,b). In the majority of the region surrounding MCC's sub-horizontal strain in the ductile crust is expected to dominate and supply the crustal mass necessary to balance rapid exhumation (Tirel et al., 2008; Wu et al., 2015, 2016). Sub-vertical strain organization in a transverse isotropy (or hexagonal symmetry) paradigm would likely produce a negative radial anisotropy signal locally beneath the MCC's, or at least diminish the regionally prevalent positive radial anisotropy due to spatial averaging of complex structural transitions (e.g., Okaya et al., 2018). However, we generally do not find distinctly weaker or negative radial anisotropy beneath the three MCC's. Instead, they generally exhibit positive radial anisotropy in the middle crust and weaker radial anisotropy in the lower crust, similar to the surrounding region. The 70-km spacing of the TA may limit detection of local V_S variations in the middle-to-lower crust beneath the Snake Range and ARG, but the dense ~5-10 km spacing of the RMSE array is capable of resolving distinctive local V_S structure if it exists beneath the Ruby Mountains. Additionally, we note that the available seismic sampling is sufficient to detect locally higher upper crustal isotropic V_S associated with all three MCC's. To explain the absence of distinctive structure (V_S and anisotropy) in the middle-to-lower crust, we suggest that ductile deformation promoted by a hot geotherm during and after middle Miocene regional scale extension of the Basin and Range effectively homogenized deep crustal V_S structure near the MCC's.

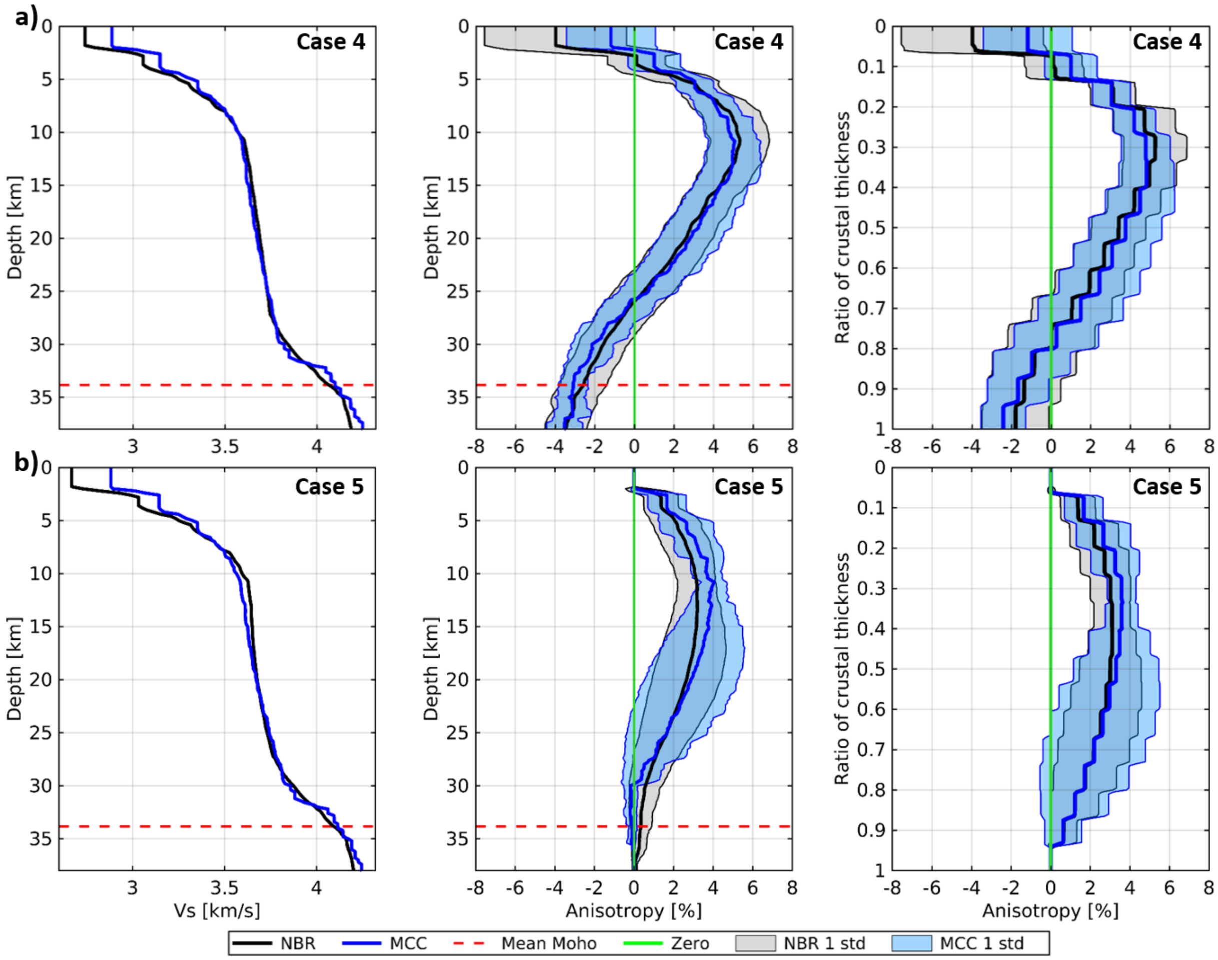

Figure 10. Comparison of V_S structure beneath MCC's and the surrounding region. (a) Left panel shows mean isotropic V_S profiles of the regional northern Basin and Range (black lines) and subset MCC's (blue lines). Notice high V_S in the upper crust of the MCC profile relative to the northern Basin and Range. Center panel shows mean crustal radial anisotropy depth profiles of the regional northern Basin and Range (black lines) and subset MCC's (blue lines) from inversion cases 4. Shaded gray and blue regions are 1 sigma corridors of the northern Basin and Range and subset MCC's, respectively. Notice similarity in magnitude and distribution between the northern Basin and Range and MCC profiles. There are relatively few profiles that extend to depths greater than 35 km and therefore the number of measurements included in the mean profile decreases with increasing depth. In the absence of depth averaging the ~5% peak magnitude of anisotropy observed here surpasses the depth averaged middle crust mean radial anisotropy of the map area, $\bar{\mathbf{x}}$ = 4.16%, as reported in Fig 7b. Right panel is same as center panel but normalized to crustal thickness. Notice largely isotropic behavior of lower crust relative to the middle crust. (b) Same as (a) but for inversion case 5. Anisotropy peaks in the middle crust in inversion cases 4 and 5 demonstrating similarity in the depth distribution of anisotropy.

5.3 Concentration of anisotropy in a middle crustal channel

Prior studies established the presence of positive radial anisotropy in the Basin and Range crust (Moschetti et al., 2010a; Xie et al., 2015). One of the main goals of this study is to evaluate potential depth dependence of radial anisotropy to provide insight regarding the deformation regimes and compositions that are most likely to contribute to the development of large-scale crustal radial anisotropy. The results from several different inversion parameterization tests provide evidence that the Rayleigh-Love discrepancy in the northeastern Basin and Range is most simply addressed by a channel of positive radial anisotropy in the middle crust from ~6-22 km depth (Fig. 9 & 10). By simplicity we mean that radial anisotropy is only required in a subset of the crust and that a relatively small magnitude of anisotropy is sufficient to simultaneously fit the Rayleigh and Love wave dispersion data (Fig. 4 & 5).

Below we consider potential reasons why radial anisotropy may be focused at middle crustal depths by discussing the potential roles of depth-dependent crustal composition and rheology. Mineral composition is a key consideration because it controls the potential magnitude of CPO development and predicts how a particular strain orientation would manifest itself in measurements of seismic radial anisotropy (e.g., Ward et al., 2012; Erdman et al., 2013). A conventional perspective is that the middle crust has an intermediate bulk composition largely containing amphibolite facies rocks and the lower crust has a mafic-to-intermediate bulk composition largely containing granulite facies rocks (Rudnick and Fountain, 1995). However, the prevalence of relatively mafic lower continental crust remains a subject of debate (Hacker et al., 2015). Rheology is expected to vary with depth from an elastic upper crust that hosts frictional fault-controlled deformation to a time-dependent ductile middle-to-lower crust that hosts flow within shear zones or distributed throughout larger volumes (e.g., Kohlstedt et al., 1995; Bürgmann and Dresen, 2008; Thatcher and Pollitz, 2008). Composition and rheology are used here as a framework for discussion but they are not independent. They are strongly linked by depth-dependent temperature and pressure conditions that change the relevant constitutive relationships and determine the stability of specific minerals.

From a compositional perspective, studies of seismic anisotropy in the continental crust often highlight the potential importance of CPO in mica-rich foliated metamorphic rocks because they are abundant and single crystal mica is one of the most anisotropic crustal minerals (Weiss et al, 1999; Lloyd et al., 2009). Hexagonal symmetry (or transverse isotropy) is a valid assumption for single crystal mica and it remains an effective approximation for many bulk rock samples with abundant mica (e.g., Nishizawa and Yoshino, 2001; Lloyd et al., 2009; Bostock and Christensen, 2012; Erdman et al., 2013; Brownlee et al., 2017). Amphibole is another common crustal mineral with potential to contribute to spatially-averaged crustal seismic anisotropy (Tatham et al., 2008; Brownlee et al., 2017). However, single crystal amphiboles are much less anisotropic than micas, and amphibole-rich rocks commonly exhibit a component of orthorhombic symmetry (Brownlee et al., 2017) which would not be accurately represented with radial anisotropy. Quartz, in aggregate, is not likely to develop strong CPO in high strain environments (Rahl and Skemer, 2016) but it can destructively interfere with bulk anisotropy in lithologies with mica or amphibole (Ward et al., 2012). Mica-bearing metamorphic rocks are generally abundant in the middle crust and rock samples exhumed from the Ruby Mountains MCC exhibit ~4-19% V_S anisotropy that is positively correlated with mica content (Erdman et al., 2013).

We suggest that mica-bearing metamorphic rocks with a sub-horizontal foliation (sub-vertical slow-axis symmetry) are a viable explanation for the observed middle crustal positive radial anisotropy signal. Geodynamic models of regional-scale extension including core complex development (Wu et al., 2015, 2016; Tirel et al., 2008) and seismic reflection imaging support the prevalence of sub-horizontal fabrics in the middle crust due to low-angle detachment faults and shear zones (Klemperer et al., 1986; McCarthy, 1986; Hauser et al., 1987; Holbrook et al., 1991; Valasek et al., 1989; Stoerzel and Smithson, 1998). Weaker radial anisotropy in the lower crust is consistent with the interpretation that mica-bearing metamorphic rocks are a major contributor to the middle crustal channel of positive radial anisotropy. This is because higher temperatures (>600-700° C) approaching the Moho would lead to diminished abundance of hydrous phases like micas in granulite facies lower crust (e.g., Mahan, 2006).

Rheological variations with depth may also contribute to the depth-dependent radial anisotropy in the study area. At geological time scales ductile flow is expected in the middle and lower crust of the Miocene-to-present Basin and Range (e.g., Thatcher and Pollitz, 2008; Tirel et al., 2008). However, decreasing shear stress and effective viscosity with depth, and increasing temperature with depth, could alter the potential for generation of large-scale seismic anisotropy. Onset of dislocation creep at lower stress conditions in the hotter lower crust favors larger dynamically recrystallized grain sizes and more distributed deformation, whereas onset of creep at higher stress conditions in the middle crust favors grain size reduction that leads to weakening and strain localization (Stipp and Tullis, 2003; Behr and Platt, 2011; Cooper et al., 2017). To first order, textures, fabrics and compositions of middle and lower crustal rocks obtained from Basin and Range MCC's reflect this transition (Fig. 11; Cooper et al., 2017). Cooper et al., (2017) identified two major rheological boundaries in Basin and Range MCC's, the brittle-ductile transition (BDT) and a deeper temperature-dependent boundary referred to as the localized-distributed transition (LDT). In this context, we suggest that positive radial anisotropy may be more effectively generated in localized shear zones closer to the top of the ductile deformation region in the middle crust. A regional median heat flux of 79 mWm^{-2} (Hasterok and Chapman, 2007) and thermal conductivity between 2.2-3.3 $Wm^{-1}K^{\circ -1}$ (Whittington et al., 2009) corresponds to a geothermal gradient range of ~25-35°C/km. Taking the ~300°C isotherm as a proxy (e.g., Cooper et al., 2017) we estimate a modern BDT depth range of ~9-12 km (Fig. 11). Results indicating that the mid crustal channel of anisotropy extends above the estimated BDT, ~6 km depth, suggests preservation of anisotropy in rocks that were deformed below the BDT and have subsequently been exhumed. Decaying strength of anisotropy in the lower crust may reflect the gradual LDT below which deformation is distributed across larger volumes and recrystallization is more rapid. The ~500° C temperature of the inferred LDT in the Basin and Range is somewhat cooler than the petrologic transition to relatively mica-poor granulite facies,

~600-700° C. The similar depths of such boundaries would not likely be resolvable with dispersion data alone. Therefore, it is not feasible, based on depth alone, to determine if the rheological or compositional transition has a more important influence on radial anisotropy.

The history of magmatism in the Basin and Range is another important factor in evaluating the potential compositional and rheological origins of depth-dependent radial anisotropy. Substantial influx of mafic melt into the lower crust is expected during the voluminous Eocene-Miocene ignimbrite flare-up (e.g., Gans, 1987; Best and Christiansen, 1991). This event likely had long lasting consequences on crustal composition and rheology. Following flat-slab subduction during the Laramide orogeny the regional lithosphere was likely cooler and contained more abundant hydrous minerals (Humphreys et al., 2003), but subsequent heating and flux of melt through the lithosphere would have dehydrated the lower crust and promoted a more mafic bulk composition (Gans, 1987). A dry lower crust in the contemporary Basin and Range is consistent with a scenario in which decreasing mica content in the lower crust leads to decreasing radial anisotropy.

Mafic intrusions would have competing effects on lower crustal rheology through thermal weakening that decays with time superimposed on long-term addition of primitive basalt or cumulate compositions that are more viscous than typical intermediate composition crust (e.g., Schutt et al., 2018). Seismic reflectivity of the Basin and Range crust peaks in the middle crust but weaker sub-horizontal reflectors are still common in the lower crust and are frequently attributed to mafic intrusions (Holbrook et al., 1991; Klemperer et al., 1986; McCarthy, 1986). A more mafic lower crust following Miocene opening of the Basin and Range would complicate the possibility of a regionally extensive LDT. Expanding on this idea, the deeply exhumed rocks that Cooper et al., (2017) used to define the LDT may preferentially represent zones of weakness during MCC formation rather than modern regionally-averaged rheology. Sill-like intrusions are interpreted to contribute to strong positive radial anisotropy in active magmatic systems as a result of shape-preferred orientation (SPO) due to large V_S contrasts between partially molten and sub-solidus crustal rocks (Jaxybulatov et al., 2014; Harmon and Rychert, 2015; Jiang et al., 2018; Lynner et al., 2018). However, crystallized basaltic sills embedded in an intermediate to mafic lower crust may not have large enough velocity contrasts for SPO to cause detectable radial anisotropy (Schmandt et al., 2019). For example, strong positive radial anisotropy, ~12%, is found beneath Yellowstone caldera but older calderas beneath the Snake River Plain are underlain by relatively isotropic crust (Jiang et al., 2018).

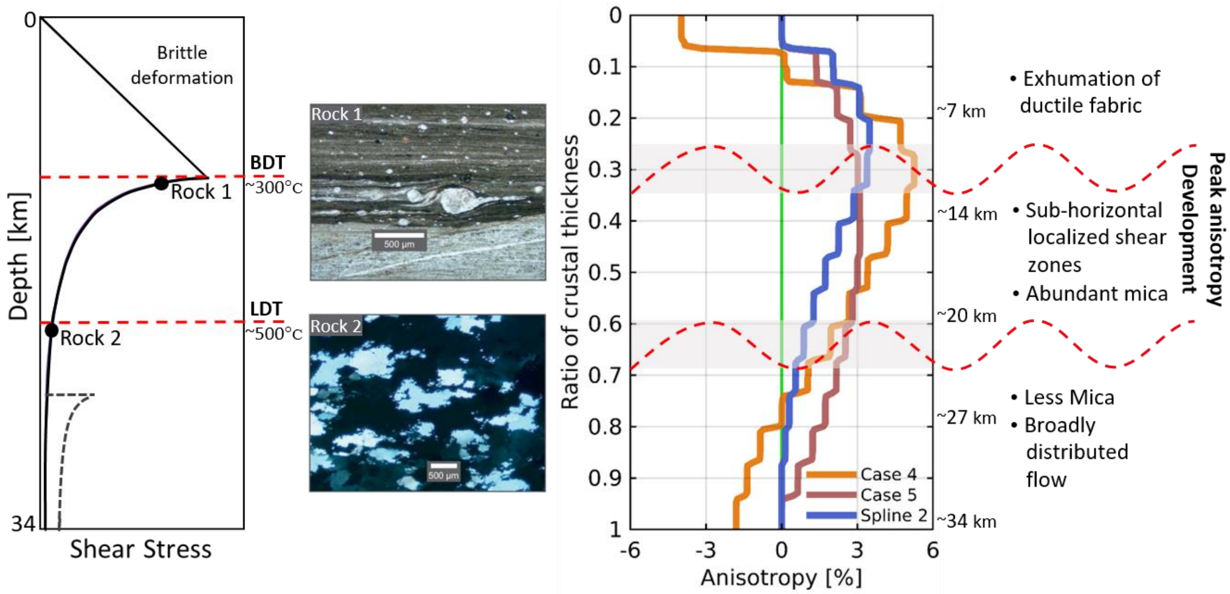

Figure 11. Synthesis of results. Left panel shows typical crustal strength profile and approximate depth ranges at which the brittle to ductile transition (BDT) and localized distributed transition (LDT) occur (dashed red line) in the Basin and Range. Possible mafic addition to the lower crust is represented with a step in the lower crust (black dashed line). Approximate temperatures of the BDT and LDT are labeled and are adopted from Cooper et al., (2017). Center shows microphotographs (originally from Platt et al., (2015) but also used in Cooper et al., (2017)) of representative middle (Rock 1) and lower (Rock 2) crustal rocks exhumed from the RMCC. Depth and stress environments from which the rocks were exhumed are labeled on crustal strength profile. As temperature increases and viscosity decreases with depth mica is lost, grains grow larger and distributed deformation diminishes anisotropy producing layering fabrics. Right panel shows study are mean anisotropy distribution with depth normalized to crustal thickness for inversion cases 4 and 5, and the inversion that allows only b-spline 2 to be anisotropic. Approximate depth ranges are labeled every 0.2 ratio of crustal thickness. Approximate depth ranges of peak anisotropy development, preservation after exhumation, and loss with increasing depth as discussed in the text are labeled to the right of center panel.

6. Conclusion

Rayleigh and Love wave dispersion measurements were inverted for radially anisotropic V_S structure of the crust and uppermost mantle beneath an area of the northeastern Basin and Range including three MCC's. Tests of several parameterizations provided new evidence that positive radial anisotropy is strongest at depths of ~8-20 km across the region. The three MCC's have distinctive high isotropic V_S in the upper crust, but they do not interrupt the regional channel of radial anisotropy focused in the middle crust. Sub-horizontal foliation (sub-vertical slow axis symmetry) of mica-bearing lithologies in ductile shear zones and detachments is a viable origin for the positive radial anisotropy focused in the middle crust. The decay of radial anisotropy with depth in the lower crust could result from decreased mica abundance as high temperatures and influx of mantle melts since the Oligocene favor a dry and increasingly mafic mean composition. Rheological transition to more broadly distributed viscous deformation at lower crustal high temperatures may also contribute to diminishing anisotropy with depth. The absence of distinctive radial anisotropy beneath the three MCC's suggests that anisotropy generated during peak metamorphism, which generally occurred in the Oligocene, was subsequently overprinted by regionally pervasive extensional deformation of the ductile crust during and after the middle Miocene. The results motivate further investigation of the depth dependence of crustal anisotropy in other areas of continental deformation to gain a global perspective on the relative importance among potential compositional and rheological contributions to crustal anisotropy.

Acknowledgements

The facilities of the Incorporated Research Institutions for Seismology (IRIS) Data Services, and specifically the IRIS Data Management Center (https://ds.iris.edu/ds/nodes/dmc/), were used for access to waveforms, related metadata, and/or derived products from seismograph networks (listed in supplemental material) used in this study. IRIS Data Services are funded through the Seismological Facilities for the Advancement of Geoscience and EarthScope Proposal of the National Science Foundation (NSF) under Cooperative Agreement EAR-1261681. S. Klemperer led the collection of the RMSE data and engaged in helpful discussions. J. Selverstone and W. Behr provided valuable feedback during the project. This research was supported by NSF EAR-1554908.

References

Almqvist, B. S., & Mainprice, D. (2017). Seismic properties and anisotropy of the continental crust: predictions based on mineral texture and rock microstructure. *Reviews of Geophysics*, *55*(2), 367-433.

Babuska, V., & Cara, M. (1991). *Seismic anisotropy in the Earth* (Vol. 10). Springer Science & Business Media.

Backus, G. E. (1962). Long-wave elastic anisotropy produced by horizontal layering. *Journal of Geophysical Research*, *67*(11), 4427-4440.

Barnes, C. G., Burton, B. R., Burling, T. C., Wright, J. E., & Karlsson, H. R. (2001). Petrology and geochemistry of the late Eocene Harrison Pass pluton, Ruby Mountains core complex, northeastern Nevada. *Journal of Petrology*, *42*(5), 901-929.

Bennett, R. A., Wernicke, B. P., Niemi, N. A., Friedrich, A. M., & Davis, J. L. (2003). Contemporary strain rates in the northern Basin and Range province from GPS data. *Tectonics*, *22*(2).

Bensen, G. D., Ritzwoller, M. H., Barmin, M. P., Levshin, A. L., Lin, F., Moschetti, M. P., Shapiro, N.M., & Yang, Y. (2007). Processing seismic ambient noise data to obtain reliable broad-band surface wave dispersion measurements. *Geophysical Journal International*, *169*(3), 1239-1260.

Best, M. G., & Christiansen, E. H. (1991). Limited extension during peak Tertiary volcanism, Great Basin of Nevada and Utah. *Journal of Geophysical Research: Solid Earth*, *96*(B8), 13509-13528.

Behr, W. M., & Platt, J. P. (2011). A naturally constrained stress profile through the middle crust in an extensional terrane. *Earth and Planetary Science Letters*, *303*(3-4), 181-192.

Brocher, T. M. (2005). Empirical relations between elastic wavespeeds and density in the Earth's crust. *Bulletin of the seismological Society of America*, *95*(6), 2081-2092.

Buehler, J. S., & Shearer, P. M. (2017). Uppermost mantle seismic velocity structure beneath USArray. *Journal of Geophysical Research: Solid Earth*, *122*(1), 436-448.

Block, L., & Royden, L. H. (1990). Core complex geometries and regional scale flow in the lower crust. *Tectonics*, *9*(4), 557-567.

Bostock, M. G., & Christensen, N. I. (2012). Split from slip and schist: Crustal anisotropy beneath northern Cascadia from non-volcanic tremor. *Journal of Geophysical Research: Solid Earth*, *117*(B8).

Brownlee, S. J., Schulte-Pelkum, V., Raju, A., Mahan, K., Condit, C., & Orlandini, O. F. (2017). Characteristics of deep crustal seismic anisotropy from a compilation of rock elasticity tensors and their expression in receiver functions. *Tectonics*, *36*(9), 1835-1857.

Bürgmann, R., & Dresen, G. (2008). Rheology of the lower crust and upper mantle: Evidence from rock mechanics, geodesy, and field observations. *Annu. Rev. Earth Planet. Sci.*, *36*, 531-567.

Camp, V. E., Pierce, K. L., & Morgan, L. A. (2015). Yellowstone plume trigger for Basin and Range extension, and coeval emplacement of the Nevada–Columbia Basin magmatic belt. *Geosphere*, *11*(2), 203-225.

Cheng, C., Chen, L., Yao, H., Jiang, M., & Wang, B. (2013). Distinct variations of crustal shear wave velocity structure and radial anisotropy beneath the North China Craton and tectonic implications. *Gondwana Research*, *23*(1), 25-38.

Christensen, N. I., & Mooney, W. D. (1995). Seismic velocity structure and composition of the continental crust: A global view. *Journal of Geophysical Research: Solid Earth*, *100*(B6), 9761-9788.

Clouzet, P., Masson, Y., & Romanowicz, B. (2018). Box Tomography: first application to the imaging of upper-mantle shear velocity and radial anisotropy structure beneath the North American continent. *Geophysical Journal International*, *213*(3), 1849-1875.

Colgan, J. P., & Henry, C. D. (2009). Rapid middle Miocene collapse of the Mesozoic orogenic plateau in north-central Nevada. *International Geology Review*, *51*(9-11), 920-961.

Colgan, J. P., Howard, K. A., Fleck, R. J., & Wooden, J. L. (2010). Rapid middle Miocene extension and unroofing of the southern Ruby Mountains, Nevada. *Tectonics*, *29*(6).

Compton, R. R., Todd, V. R., Zartman, R. E., & Naeser, C. W. (1977). Oligocene and Miocene metamorphism, folding, and low-angle faulting in northwestern Utah. *Geological Society of America Bulletin*, *88*(9), 1237-1250.

Coney, P. J., & Harms, T. A. (1984). Cordilleran metamorphic core complexes: Cenozoic extensional relics of Mesozoic compression. *Geology*, *12*(9), 550-554.

Cooper, F. J., Platt, J. P., & Behr, W. M. (2017). Rheological transitions in the middle crust: insights from Cordilleran metamorphic core complexes. *Solid Earth*, *8*(1), 199-215.

Crampin, S. (1994). The fracture criticality of crustal rocks. *Geophysical Journal International*, *118*(2), 428-438.

Crittenden, M. D., Coney, P. J., Davis, G. H., & Davis, G. H. (Eds.). (1980). *Cordilleran metamorphic core complexes* (Vol. 153). Geological Society of America.

Dalton, C. A., & Gaherty, J. B. (2013). Seismic anisotropy in the continental crust of northwestern Canada. *Geophysical Journal International*, *193*(1), 338-348.

Delph, J. R., Levander, A., & Niu, F. (2019). Constraining crustal properties using receiver functions and the autocorrelation of earthquake-generated body waves. *Journal of Geophysical Research: Solid Earth*.

Dewey, J. F. (1988). Extensional collapse of orogens. *Tectonics*, *7*(6), 1123-1139.

Dreiling, J., Tilmann, F., Yuan, X., Giese, J., Rindraharisaona, E. J., Rümpker, G., & Wysession, M. E. (2018). Crustal Radial Anisotropy and Linkage to Geodynamic Processes: A Study Based on Seismic Ambient Noise in Southern Madagascar. *Journal of Geophysical Research: Solid Earth*, *123*(6), 5130-5146.

Duret, F., Shapiro, N. M., Cao, Z., Levin, V., Molnar, P., & Roecker, S. (2010). Surface wave dispersion across Tibet: Direct evidence for radial anisotropy in the crust. *Geophysical Research Letters*, *37*(16).

Dziewonski, A. M., & Anderson, D. L. (1981). Preliminary reference Earth model. *Physics of the earth and planetary interiors*, *25*(4), 297-356.

Egger, A. E., Dumitru, T. A., Miller, E. L., Savage, C. F., & Wooden, J. L. (2003). Timing and nature of Tertiary plutonism and extension in the Grouse Creek Mountains, Utah. *International Geology Review*, *45*(6), 497-532.

Ekström, G., Abers, G. A., & Webb, S. C. (2009). Determination of surface-wave phase velocities across USArray from noise and Aki's spectral formulation. *Geophysical Research Letters*, *36*(18).

Ekström, G. (2017). Short-period surface-wave phase velocities across the conterminous United States. *Physics of the Earth and Planetary Interiors*, *270*, 168-175.

Erdman, M. E., Hacker, B. R., Zandt, G., & Seward, G. (2013). Seismic anisotropy of the crust: electron-backscatter diffraction measurements from the Basin and Range. *Geophysical Journal International*, *195*(2), 1211-1229.

Feng, L., & Ritzwoller, M. H. (2019). A 3-D shear velocity model of the crust and uppermost mantle beneath Alaska including apparent radial anisotropy. *Journal of Geophysical Research: Solid Earth*.

Fenneman, N. M. (1917). Physiographic subdivision of the United States. *Proceedings of the National Academy of Sciences of the United States of America*, *3*(1), 17.

Fu, Y. V., & Li, A. (2015). Crustal shear wave velocity and radial anisotropy beneath the Rio Grande rift from ambient noise tomography. *Journal of Geophysical Research: Solid Earth*, *120*(2), 1005-1019.

Gans, P. B. (1987). An open-system, two-layer crustal stretching model for the eastern Great Basin. *Tectonics*, *6*(1), 1-12.

Gao, C., & Lekić, V. (2018). Consequences of parametrization choices in surface wave inversion: insights from transdimensional Bayesian methods. *Geophysical Journal International*, *215*(2), 1037-1063.
Gébelin, A., Mulch, A., Teyssier, C., Heizler, M., Vennemann, T., & Seaton, N. C. (2011). Oligo-Miocene extensional tectonics and fluid flow across the Northern Snake Range detachment system, Nevada. *Tectonics*, *30*(5).
Gilbert, H. (2012). Crustal structure and signatures of recent tectonism as influenced by ancient terranes in the western United States. *Geosphere*, *8*(1), 141-157.
Gorbatov, A., Saygin, E., & Kennett, B. L. N. (2012). Crustal properties from seismic station autocorrelograms. *Geophysical Journal International*, *192*(2), 861-870.
Hacker, B. R., Ritzwoller, M. H., & Xie, J. (2014). Partially melted, mica-bearing crust in Central Tibet. *Tectonics*, *33*(7), 1408-1424.
Hacker, B. R., Kelemen, P. B., & Behn, M. D. (2015). Continental lower crust. *Annual Review of Earth and Planetary Sciences*, *43*, 167-205.
Haines, S. H., & van der Pluijm, B. A. (2010). Dating the detachment fault system of the Ruby Mountains, Nevada: Significance for the kinematics of low-angle normal faults. *Tectonics*, *29*(4).
Hamilton, W., & Myers, W. B. (1966). Cenozoic tectonics of the western United States. *Reviews of Geophysics*, *4*(4), 509-549.
Hammond, W. C., & Thatcher, W. (2004). Contemporary tectonic deformation of the Basin and Range province, western United States: 10 years of observation with the Global Positioning System. *Journal of Geophysical Research: Solid Earth*, *109*(B8).
Hansen, S. M., Dueker, K., & Schmandt, B. (2015). Thermal classification of lithospheric discontinuities beneath USArray. *Earth and Planetary Science Letters*, *431*, 36-47.
Harmon, N., & Rychert, C. A. (2015). Seismic imaging of deep crustal melt sills beneath Costa Rica suggests a method for the formation of the Archean continental crust. *Earth and Planetary Science Letters*, *430*, 140-148.
Hasterok, D., & Chapman, D. S. (2007). Continental thermal isostasy: 2. Application to North America. *Journal of Geophysical Research: Solid Earth*, *112*(B6).
Hastings, W. K. (1970). Monte Carlo sampling methods using Markov chains and their applications.
Hauser, E., Potter, C., Hauge, T., Burgess, S., Burtch, S., Mutschler, J., Allmendinger, R., Brown, L., Kaufman, S., & Oliver, J. (1987). Crustal structure of eastern Nevada from COCORP deep seismic reflection data. *Geological Society of America Bulletin*, *99*(6), 833-844.
Herrmann, R. B. (2013). Computer programs in seismology: An evolving tool for instruction and research. *Seismological Research Letters*, *84*(6), 1081-1088.
Hodges, K. V., Snoke, A. W., & Hurlow, H. A. (1992). Thermal evolution of a portion of the Sevier hinterland: the northern Ruby Mountains-East Humboldt Range and Wood Hills, northeastern Nevada. *Tectonics*, *11*(1), 154-164.

Holbrook, W. S., Catchings, R. D., & Jarchow, C. M. (1991). Origins of deep crustal reflections: Implications of coincident seismic refraction and reflection data in Nevada. *Geology*, *19*(2), 175-179.

Huang, H., Yao, H., & van der Hilst, R. D. (2010). Radial anisotropy in the crust of SE Tibet and SW China from ambient noise interferometry. *Geophysical Research Letters*, *37*(21).

Humphreys, E., Hessler, E., Dueker, K., Farmer, G. L., Erslev, E., & Atwater, T. (2003). How Laramide-age hydration of North American lithosphere by the Farallon slab controlled subsequent activity in the western United States. *International Geology Review*, *45*(7), 575-595.

Jaxybulatov, K., Shapiro, N. M., Koulakov, I., Mordret, A., Landès, M., & Sens-Schoenfelder, C. (2014). A large magmatic sill complex beneath the Toba caldera. *science*, *346*(6209), 617-619.

Jiang, C., Schmandt, B., Farrell, J., Lin, F. C., & Ward, K. M. (2018). Seismically anisotropic magma reservoirs underlying silicic calderas. *Geology*, *46*(8), 727-730.

Klemperer, S. L., Hauge, T. A., Hauser, E. C., Oliver, J. E., & Potter, C. J. (1986). The Moho in the northern Basin and Range province, Nevada, along the COCORP 40 N seismic-reflection transect. *Geological Society of America Bulletin*, *97*(5), 603-618.

Kohlstedt, D. L., Evans, B., & Mackwell, S. J. (1995). Strength of the lithosphere: Constraints imposed by laboratory experiments. *Journal of Geophysical Research: Solid Earth*, *100*(B9), 17587-17602.

Konstantinou, A., Strickland, A., Miller, E., Vervoort, J., Fisher, C. M., Wooden, J., & Valley, J. (2013). Synextensional magmatism leading to crustal flow in the Albion–Raft River–Grouse Creek metamorphic core complex, northeastern Basin and Range. *Tectonics*, *32*(5), 1384-1403.

Kreemer, C., Blewitt, G., & Klein, E. C. (2014). A geodetic plate motion and Global Strain Rate Model. *Geochemistry, Geophysics, Geosystems*, *15*(10), 3849-3889.

Laske, G., Masters, G., Ma, Z., & Pasyanos, M. (2013, April). Update on CRUST1. 0—A 1-degree global model of Earth’s crust. In *Geophys. Res. Abstr* (Vol. 15, p. 2658). Vienna, Austria: EGU General Assembly.

Leary, P. C., Crampin, S., & McEvilly, T. V. (1990). Seismic fracture anisotropy in the Earth's crust: An overview. *Journal of Geophysical Research: Solid Earth*, *95*(B7), 11105-11114.

Lee, J., Miller, E. L., & Sutter, J. F. (1987). Ductile strain and metamorphism in an extensional tectonic setting: A case study from the northern Snake Range, Nevada, USA. *Geological Society, London, Special Publications*, *28*(1), 267-298.

Lekić, V., & Fischer, K. M. (2014). Contrasting lithospheric signatures across the western United States revealed by Sp receiver functions. *Earth and Planetary Science Letters*, *402*, 90-98.

Levander, A., & Miller, M. S. (2012). Evolutionary aspects of lithosphere discontinuity structure in the western US. *Geochemistry, Geophysics, Geosystems*, *13*(7).

Lin, F. C., Tsai, V. C., & Schmandt, B. (2014). 3-D crustal structure of the western United States: application of Rayleigh-wave ellipticity extracted from noise cross-correlations. *Geophysical Journal International*, *198*(2), 656-670.

Lin, F. C., Ritzwoller, M. H., Yang, Y., Moschetti, M. P., & Fouch, M. J. (2011). Complex and variable crustal and uppermost mantle seismic anisotropy in the western United States. *Nature Geoscience*, *4*(1), 55.

Lin, F. C., Moschetti, M. P., & Ritzwoller, M. H. (2008). Surface wave tomography of the western United States from ambient seismic noise: Rayleigh and Love wave phase velocity maps. *Geophysical Journal International*, *173*(1), 281-298.

Litherland, M. M., & Klemperer, S. L. (2017). Crustal structure of the Ruby Mountains metamorphic core complex, Nevada, from passive seismic imaging. *Geosphere*, *13*(5), 1506-1523.

Lloyd, G. E., Butler, R. W., Casey, M., & Mainprice, D. (2009). Mica, deformation fabrics and the seismic properties of the continental crust. *Earth and Planetary Science Letters*, *288*(1-2), 320-328.

Long, S. P. (2018). Geometry and magnitude of extension in the Basin and Range Province (39° N), Utah, Nevada, and California, USA: Constraints from a province-scale cross section. *Bulletin*, *131*(1-2), 99-119.

Lowry, A. R., & Pérez-Gussinyé, M. (2011). The role of crustal quartz in controlling Cordilleran deformation. *Nature*, *471*(7338), 353.

Luo, Y., Xu, Y., & Yang, Y. (2013). Crustal radial anisotropy beneath the Dabie orogenic belt from ambient noise tomography. *Geophysical Journal International*, *195*(2), 1149-1164.

Lynner, C., Beck, S. L., Zandt, G., Porritt, R. W., Lin, F. C., & Eilon, Z. C. (2018). Midcrustal deformation in the Central Andes constrained by radial anisotropy. *Journal of Geophysical Research: Solid Earth*, *123*(6), 4798-4813.

MacCready, T., Snoke, A. W., Wright, J. E., & Howard, K. A. (1997). Mid-crustal flow during Tertiary extension in the Ruby Mountains core complex, Nevada. *Geological Society of America Bulletin*, *109*(12), 1576-1594.

Mahan, K. (2006). Retrograde mica in deep crustal granulites: Implications for crustal seismic anisotropy. *Geophysical research letters*, *33*(24).

Mainprice, D., & Nicolas, A. (1989). Development of shape and lattice preferred orientations: application to the seismic anisotropy of the lower crust. *Journal of Structural Geology*, *11*(1-2), 175-189.

Matharu, G., Bostock, M. G., Christensen, N. I., & Tromp, J. (2014). Crustal anisotropy in a subduction zone forearc: Northern Cascadia. *Journal of Geophysical Research: Solid Earth*, *119*(9), 7058-7078.

McCarthy, J. (1986). Reflection profiles from the Snake Range metamorphic core complex: A window into the mid-crust. *Reflection seismology: The continental crust*, *14*, 281-292.

McCarthy, J. & Thompson, G. A. (1988). Seismic imaging of extended crust with emphasis on the western United States. *Geological Society of America Bulletin*, *100*(9), 1361-1374.

McQuarrie, N., & Wernicke, B. P. (2005). An animated tectonic reconstruction of southwestern North America since 36 Ma. *Geosphere*, *1*(3), 147-172.

Mikulich, M. J., & Smith, R. B. (1974). Seismic reflection and aeromagnetic surveys of the Great Salt Lake, Utah. *Geological Society of America Bulletin*, *85*(6), 991-1002.

Miller, E. L., Dumitru, T. A., Brown, R. W., & Gans, P. B. (1999). Rapid Miocene slip on the Snake Range–Deep Creek range fault system, east-central Nevada. *Geological Society of America Bulletin*, *111*(6), 886-905.

Moschetti, M. P., Ritzwoller, M. H., Lin, F., & Yang, Y. (2010a). Seismic evidence for widespread western-US deep-crustal deformation caused by extension. *Nature*, *464*(7290), 885.

Moschetti, M. P., Ritzwoller, M. H., Lin, F. C., & Yang, Y. (2010b). Crustal shear wave velocity structure of the western United States inferred from ambient seismic noise and earthquake data. *Journal of Geophysical Research: Solid Earth*, *115*(B10).

Mosegaard, K., & Tarantola, A. (1995). Monte Carlo sampling of solutions to inverse problems. *Journal of Geophysical Research: Solid Earth*, *100*(B7), 12431-12447.

Nishizawa, O., & Yoshino, T. (2001). Seismic velocity anisotropy in mica-rich rocks: An inclusion model. *Geophysical Journal International*, *145*(1), 19-32.

Ojo, A. O., Ni, S., & Li, Z. (2017). Crustal radial anisotropy beneath Cameroon from ambient noise tomography. *Tectonophysics*, *696*, 37-51.

Okaya, D., Vel, S. S., Song, W. J., & Johnson, S. E. (2018). Modification of crustal seismic anisotropy by geological structures ("structural geometric anisotropy"). *Geosphere*, *15*(1), 146-170.

Panning, M., & Romanowicz, B. (2006). A three-dimensional radially anisotropic model of shear velocity in the whole mantle. Geophysical Journal International, 167(1), 361-379.

Pérouse, E., & Wernicke, B. P. (2017). Spatiotemporal evolution of fault slip rates in deforming continents: The case of the Great Basin region, northern Basin and Range province. *Geosphere*, *13*(1), 112-135.

Platt, J. P., Behr, W. M., & Cooper, F. J. (2015). Metamorphic core complexes: windows into the mechanics and rheology of the crust. *Journal of the Geological Society*, *172*(1), 9-27.

Rahl, J. M., & Skemer, P. (2016). Microstructural evolution and rheology of quartz in a mid-crustal shear zone. *Tectonophysics*, *680*, 129-139

Rey, P. F., Teyssier, C., & Whitney, D. L. (2009a). Extension rates, crustal melting, and core complex dynamics. *Geology*, *37*(5), 391-394.

Rey, P. F., Teyssier, C., & Whitney, D. L. (2009b). The role of partial melting and extensional strain rates in the development of metamorphic core complexes. *Tectonophysics*, *477*(3-4), 135-144.

Rey, P., Vanderhaeghe, O., & Teyssier, C. (2001). Gravitational collapse of the continental crust: definition, regimes and modes. *Tectonophysics*, *342*(3-4), 435-449.

Rudnick, R. L., & Fountain, D. M. (1995). Nature and composition of the continental crust: a lower crustal perspective. *Reviews of geophysics*, *33*(3), 267-309.

Sabra, K. G., Gerstoft, P., Roux, P., Kuperman, W. A., & Fehler, M. C. (2005). Extracting time-domain Green's function estimates from ambient seismic noise. *Geophysical Research Letters*, *32*(3).

Schellart, W. P., Stegman, D. R., Farrington, R. J., Freeman, J., & Moresi, L. (2010). Cenozoic tectonics of western North America controlled by evolving width of Farallon slab. *Science*, *329*(5989), 316-319.

Schmandt, B., Lin, F. C., & Karlstrom, K. E. (2015). Distinct crustal isostasy trends east and west of the Rocky Mountain Front. *Geophysical Research Letters*, *42*(23), 10-290.

Schmandt, B., Jiang, C., & Farrell, J. (2019). Seismic perspectives from the western US on magma reservoirs underlying large silicic calderas. *Journal of Volcanology and Geothermal Research*.

Schutt, D. L., Lowry, A. R., & Buehler, J. S. (2018). Moho temperature and mobility of lower crust in the western United States. *Geology*, *46*(3), 219-222.

Seats, K. J., Lawrence, J. F., & Prieto, G. A. (2012). Improved ambient noise correlation functions using Welch′ s method. *Geophysical Journal International*, *188*(2), 513-523.

Shapiro, N. M., & Campillo, M. (2004). Emergence of broadband Rayleigh waves from correlations of the ambient seismic noise. *Geophysical Research Letters*, *31*(7).

Shapiro, N. M., Ritzwoller, M. H., Molnar, P., & Levin, V. (2004). Thinning and flow of Tibetan crust constrained by seismic anisotropy. *Science*, *305*(5681), 233-236.

Shen, W., Ritzwoller, M. H., Schulte-Pelkum, V., & Lin, F. C. (2012). Joint inversion of surface wave dispersion and receiver functions: a Bayesian Monte-Carlo approach. *Geophysical Journal International*, *192*(2), 807-836.

Shen, W., & Ritzwoller, M. H. (2016). Crustal and uppermost mantle structure beneath the United States. *Journal of Geophysical Research: Solid Earth*, *121*(6), 4306-4342.

Sherrington, H. F., Zandt, G., & Frederiksen, A. (2004). Crustal fabric in the Tibetan Plateau based on waveform inversions for seismic anisotropy parameters. *Journal of Geophysical Research: Solid Earth*, *109*(B2).

Shirzad, T., & Shomali, Z. H. (2014). Shallow crustal radial anisotropy beneath the Tehran basin of Iran from seismic ambient noise tomography. *Physics of the Earth and Planetary Interiors*, *231*, 16-29.

Stipp, M., & Tullis, J. (2003). The recrystallized grain size piezometer for quartz. *Geophysical Research Letters*, *30*(21).

Stoerzel, A., & Smithson, S. B. (1998). Two-dimensional travel time inversion for the crustal P and S wave velocity structure of the Ruby Mountains metamorphic core complex, NE Nevada. *Journal of Geophysical Research: Solid Earth*, *103*(B9), 21121-21143.

Sullivan, W. A., & Snoke, A. W. (2007). Comparative anatomy of core-complex development in the northeastern Great Basin, USA. *Rocky Mountain Geology*, *42*(1), 1-29.

Tatham, D. J., Lloyd, G. E., Butler, R. W. H., & Casey, M. (2008). Amphibole and lower crustal seismic properties. *Earth and Planetary Science Letters*, *267*(1-2), 118-128.

Tesauro, M., Kaban, M. K., Mooney, W. D., & Cloetingh, S. (2014). NACr14: A 3D model for the crustal structure of the North American Continent. *Tectonophysics, 631*, 65-86.

Thatcher, W., & Pollitz, F. F. (2008). Temporal evolution of continental lithospheric strength in actively deforming regions. *GSA TODAY*, *18*(4/5), 4.

Tibuleac, I. M., & von Seggern, D. (2012). Crust-mantle boundary reflectors in Nevada from ambient seismic noise autocorrelations. *Geophysical Journal International*, *189*(1), 493-500.

Tirel, C., Brun, J. P., & Burov, E. (2008). Dynamics and structural development of metamorphic core complexes. *Journal of Geophysical Research: Solid Earth*, *113*(B4).

Tsai, V. C., & Moschetti, M. P. (2010). An explicit relationship between time-domain noise correlation and spatial autocorrelation (SPAC) results. *Geophysical Journal International*, *182*(1), 454-460.

Valasek, P. A., Snoke, A. W., Hurich, C. A., & Smithson, S. B. (1989). Nature and origin of seismic reflection fabric, Ruby-East Humboldt metamorphic core complex, Nevada. *Tectonics*, *8*(2), 391-415.

Wang, K., Liu, Q., & Yang, Y. (2018, December). Crustal Radial Anisotropy of Southern California Revealed by Multi-component Ambient Noise Adjoint Tomography. In *AGU Fall Meeting Abstracts*.

Ward, D., Mahan, K., & Schulte-Pelkum, V. (2012). Roles of quartz and mica in seismic anisotropy of mylonites. *Geophysical Journal International*, *190*(2), 1123-1134.

Weiss, T., Siegesmund, S., Rabbel, W., Bohlen, T., & Pohl, M. (1999). Seismic velocities and anisotropy of the lower continental crust: a review. In *Seismic Exploration of the Deep Continental Crust* (pp. 97-122). Birkhäuser, Basel.

Wells, M. L., Snee, L. W., & Blythe, A. E. (2000). Dating of major normal fault systems using thermochronology: An example from the Raft River detachment, Basin and Range, western United States. *Journal of Geophysical Research: Solid Earth*, *105*(B7), 16303-16327.

Wernicke, B., & Snow, J. K. (1998). Cenozoic tectonism in the central Basin and Range: Motion of the Sierran-Great Valley block. *International Geology Review*, *40*(5), 403-410.

Wernicke, B., Axen, G. J., & Snow, J. K. (1988). Basin and Range extensional tectonics at the latitude of Las Vegas, Nevada. *Geological Society of America Bulletin*, *100*(11), 1738-1757.

Whittington, A. G., Hofmeister, A. M., & Nabelek, P. I. (2009). Temperature-dependent thermal diffusivity of the Earth’s crust and implications for magmatism. *Nature*, *458*(7236), 319-321.

Whitney, D. L., Teyssier, C., Rey, P., & Buck, W. R. (2013). Continental and oceanic core complexes. *Bulletin*, *125*(3-4), 273-298.

Wu, G., & Lavier, L. L. (2016). The effects of lower crustal strength and preexisting midcrustal shear zones on the formation of continental core complexes and low-angle normal faults. *Tectonics*, *35*(9), 2195-2214.

Wu, G., Lavier, L. L., & Choi, E. (2015). Modes of continental extension in a crustal wedge. *Earth and Planetary Science Letters*, *421*, 89-97.

Xie, J., Ritzwoller, M. H., Shen, W., & Wang, W. (2017). Crustal anisotropy across eastern Tibet and surroundings modeled as a depth-dependent tilted hexagonally symmetric medium. *Geophysical Journal International*, *209*(1), 466-491.

Xie, J., Ritzwoller, M. H., Brownlee, S. J., & Hacker, B. R. (2015). Inferring the oriented elastic tensor from surface wave observations: preliminary application across the western United States. *Geophysical Journal International*, *201*(2), 996-1021.

Xie, J., Ritzwoller, M. H., Shen, W., Yang, Y., Zheng, Y., & Zhou, L. (2013). Crustal radial anisotropy across eastern Tibet and the western Yangtze craton. *Journal of Geophysical Research: Solid Earth*, *118*(8), 4226-4252.

Yuan, H., French, S., Cupillard, P., & Romanowicz, B. (2014). Lithospheric expression of geological units in central and eastern North America from full waveform tomography. *Earth and Planetary Science Letters*, *402*, 176-186.

Zandt, G., Myers, S. C., & Wallace, T. C. (1995). Crust and mantle structure across the Basin and Range-Colorado Plateau boundary at 37 N latitude and implications for Cenozoic extensional mechanism. *Journal of Geophysical Research: Solid Earth*, *100*(B6), 10529-10548.

Zhu, H., Komatitsch, D., & Tromp, J. (2017). Radial anisotropy of the North American upper mantle based on adjoint tomography with USArray. *Geophysical Journal International*, *211*(1), 349-377.

Tectonics

Supporting Information for

A Middle Crustal Channel of Radial Anisotropy Beneath the Northeastern Basin and Range

Justin Wilgus[1], Chengxin Jiang[1*], Brandon Schmandt[1]

1. Department of Earth and Planetary Sciences, University of New Mexico, Albuquerque, NM, USA
*now at Research School of Earth Sciences, The Australian National University, Acton, ACT, Australia

Contents of this file

Introduction

The supplementary information provided here includes 10 figures and 2 tables. These materials expand on data coverage, processing, methodology, and results.

Figure S1. Interstation Rayleigh wave ray path coverage of study area.
Figure S2. Regional Love and Rayleigh wave phase velocity maps.
Figure S3. Observed and predicted Dispersion curves, and 1D BMMC inversion V_S and anisotropy results from 1-D grid point point 40.5°, -115.5°.
Figure S4. Chi-squared (χ^2) misfit maps.
Figure S5. Depth-integrated absolute value of crustal radial anisotropy maps.
Figure S6. BMMC inversion parameterization and constraint test results from 1-D grid point 40°, -116°.
Figure S7. Depth averaged isotropic V_S and radial anisotropy maps.
Figure S8. Isotropic V_S and anisotropy results from inversion case 4 without statistical culling.
Figure S9. Isotropic V_S and anisotropy results from inversion case 5 without statistical culling.
Figure S10. Isotropic V_S and anisotropy results from inversion case 5 with statistical culling.
Table S1. Summary of seismic networks used for this study.
Table S2. Rayleigh and Love wave errors.

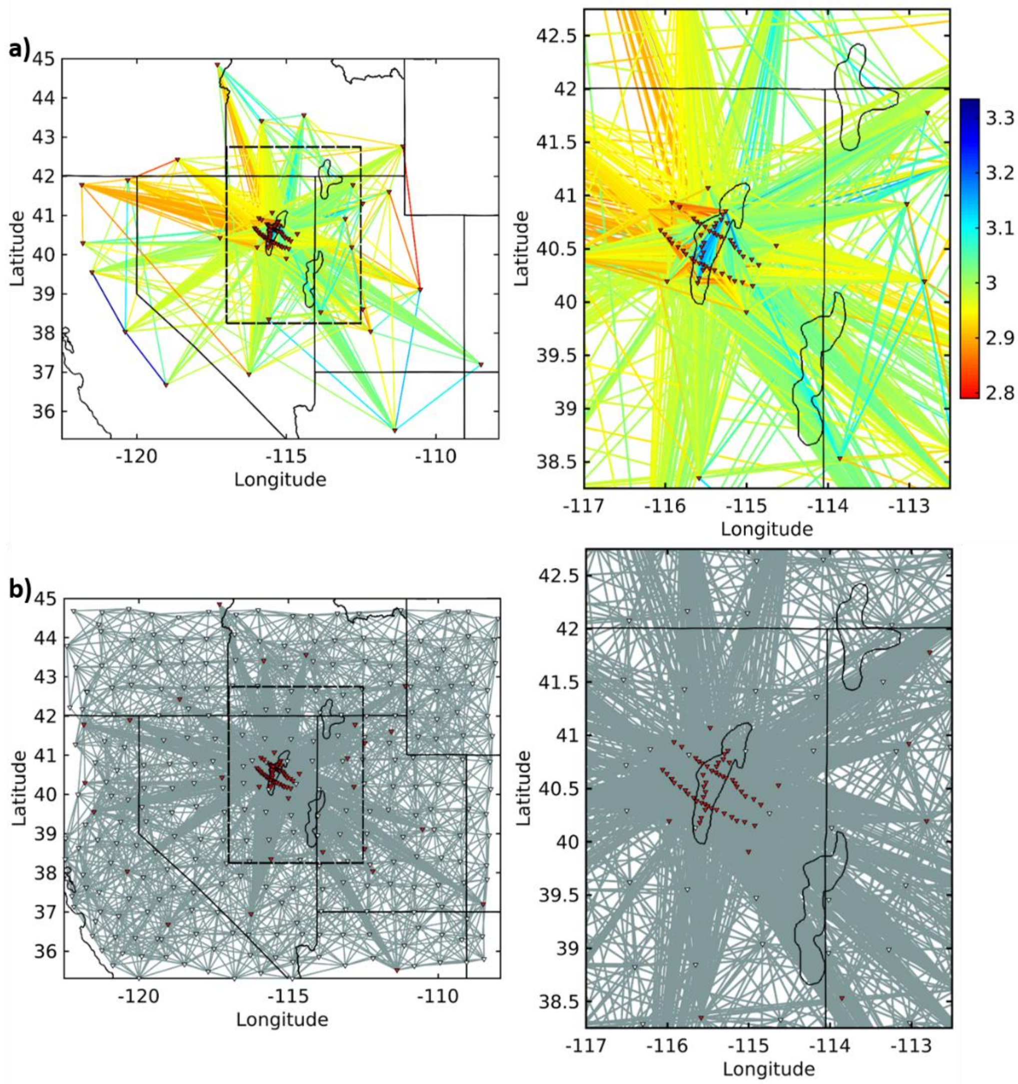

Figure S1. Interstation Rayleigh wave ray path coverage of study area retained for tomography at a 6 s period. (a) Left panel shows 1521 interstation Rayleigh wave phase velocity values calculated as a part of this study using RMSE and surrounding stations (red triangles; table 1) between 2010-2012. For Love waves 1631 interstation phase velocity values were contributed for 6 s period tomographic maps (Supplementary Information S2). Black dashes delineate study area enlarged in the right panel. Notice high density of interstation paths in the study region and high velocities that coincide with the location and strike of the RMCC. (b) Interstation Rayleigh wave phase velocity ray paths after combination with measurements from Ekström, (2017) made with TA stations between time period 2005-2008. Right panel again shows enlarged study area delineated with black dashed line in right panel. Notice increased regional path coverage and increased number of crossing paths within study region.

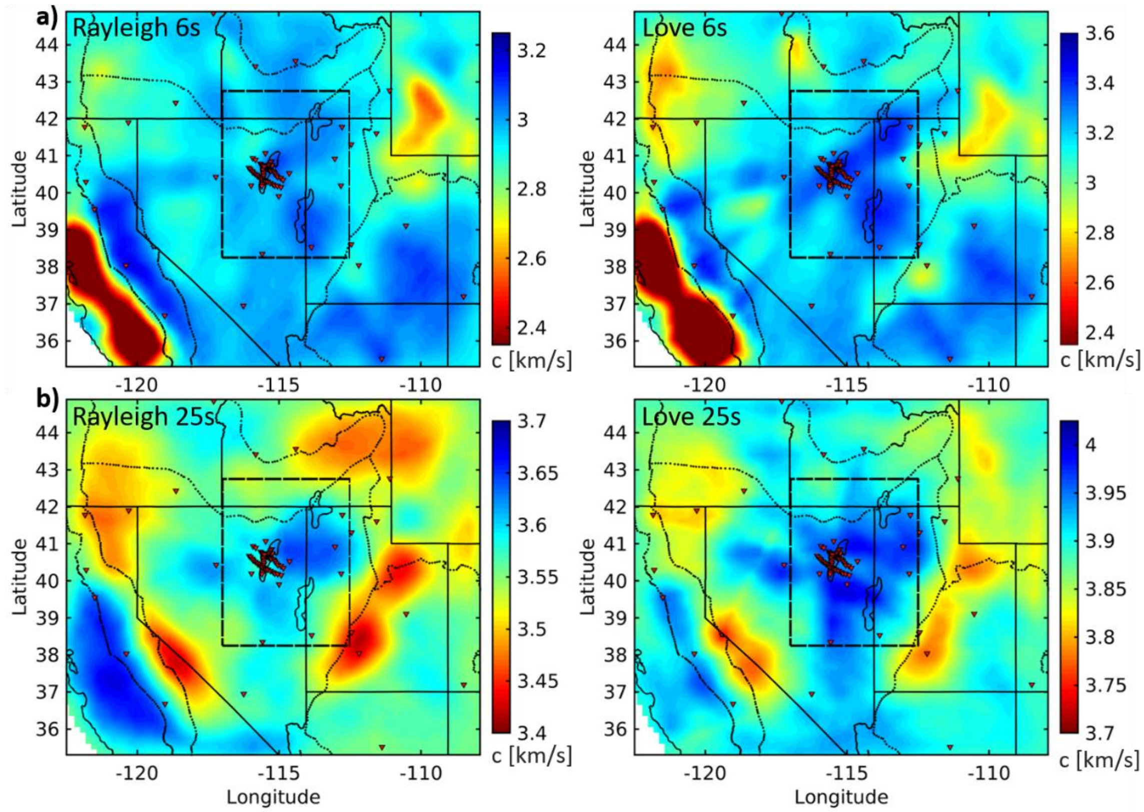

Figure S2. Regional Love and Rayleigh wave phase velocity maps. (a) 6 s period Rayleigh (left panel) and Love (right panel) wave phase velocity, c, maps. At a period of 6 s surface waves are sensitive to structures in the shallow crust. Mapped phase velocity anomalies agree with well-known geologic provinces such as the Colorado Plateau, San Joaquin valley, and the Sierra Nevada mountain range. Within the study region, particularly in Love wave maps, high velocity anomalies are coincident with the location of MCC's. (b) Same as (a) but for a period of 25 s which is sensitive to structures in the deep crust. The Basin and Range exhibits a fast phase velocity anomaly likely due to the shallow Moho allowing for sensitivity to high velocity mantle.

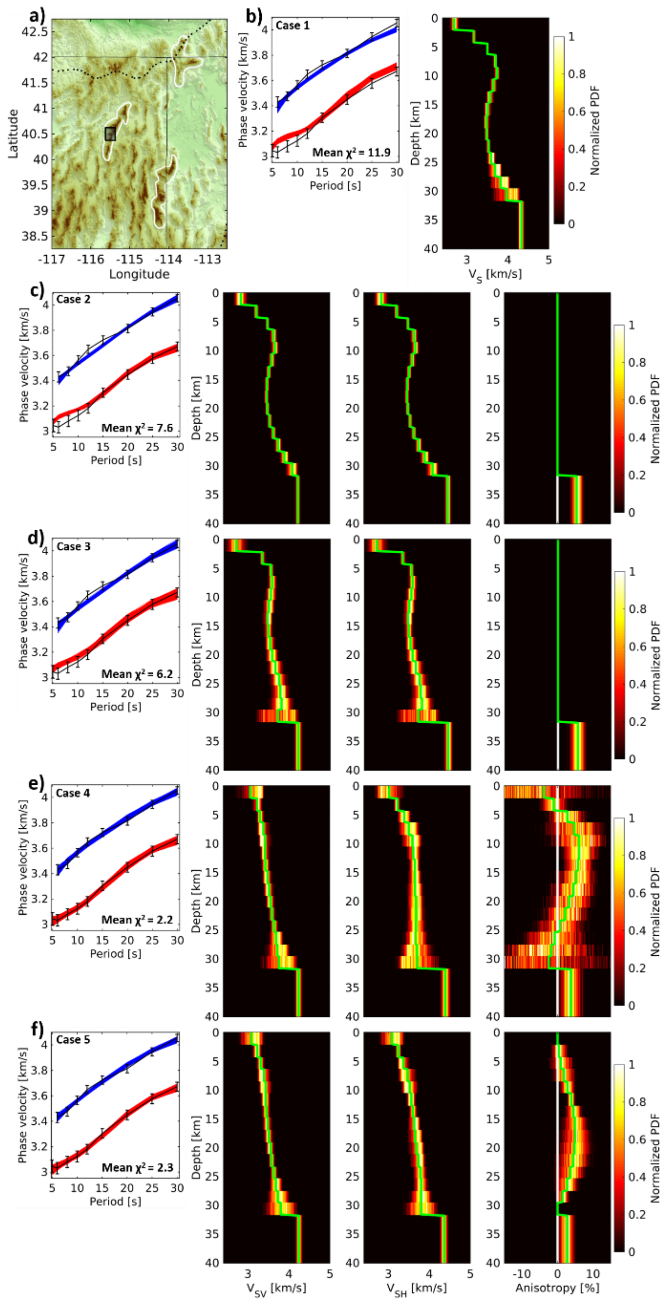

Figure S3. Observed and predicted dispersion curves and 1D BMMC inversion V_S and anisotropy results from 1-D grid point 40.5°, -115.5° centered on the southern portion of the RMCC. (a) Map showing the location of grid point area (black box). (b-f) Evolution of 1-D χ^2 dispersion misfits and V_S and anisotropy with depth for inversion cases 1-5. (b) Left panel shows observed (black lines) and predicted Love (blue lines) and Rayleigh (red lines) wave dispersion curves for inversion case 1 labeled in the upper left corner. Observation error bars are from Supplementary information table 2. Mean χ^2 dispersion misfits for each case are given in the left portion of each panel. Right panel shows the posterior probability distribution as a function of depth for V_S. Green line is the mean of the posterior distribution. (c) same as (b) but for inversion case 2 and right panels showing the posterior probability distribution as a function of depth for, V_{SV}, V_{SH}, and anisotropy. (d) same as (c) but for inversion case 3. Predicted curves for inversion cases 1-3 (b-d) do not fit observed curves well. (e) same as (f) but for inversion case 4. Notice decrease in χ^2 misfit and increase in width of 1 sigma corridor for, V_{SV}, V_{SH}, and anisotropy. (f) same as (e) but for inversion case 5. Inversion cases 4 and 5 (e, f) achieve similarly low χ^2 misfits.

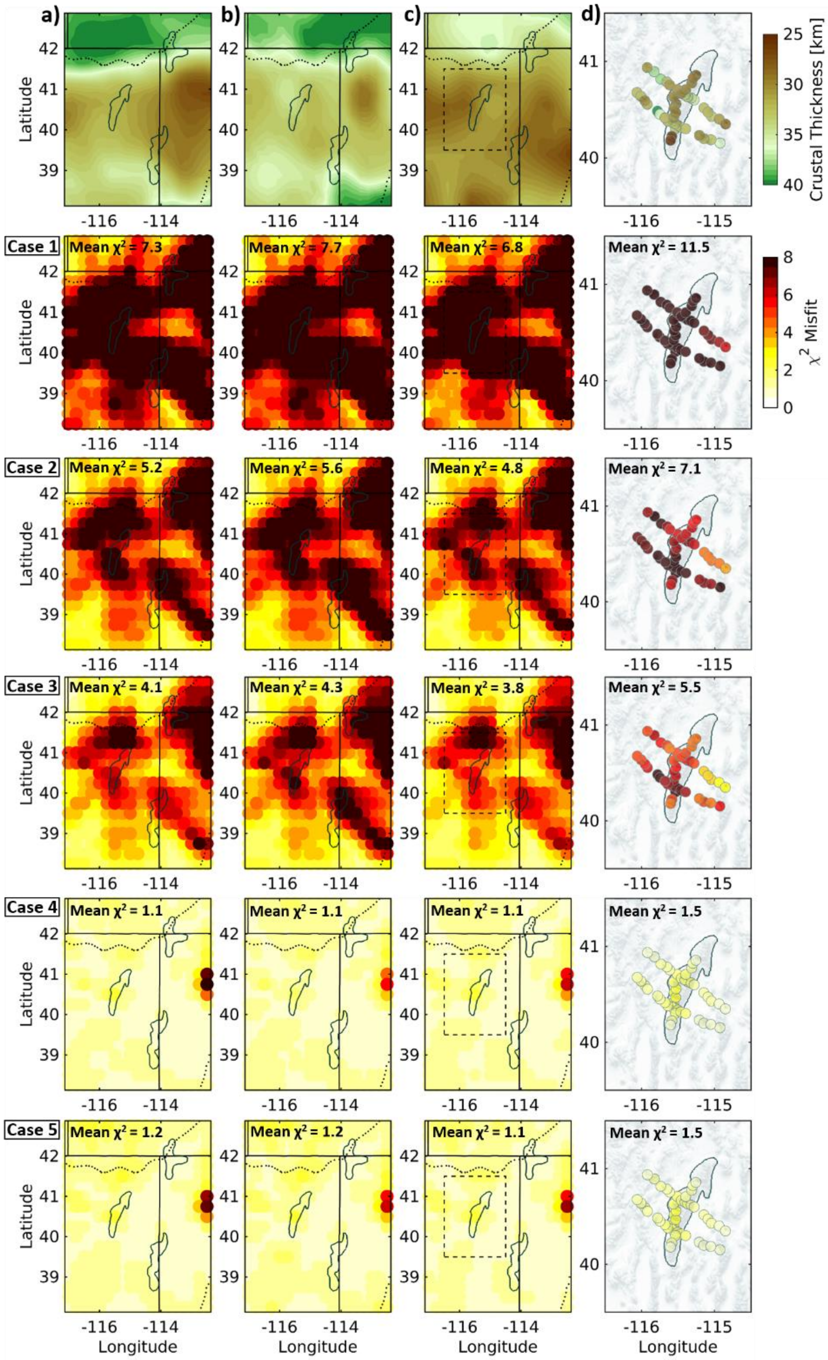

Figure S4. Chi-squared (χ^2) misfit maps of the study region for the five parameterization cases (described in section 3.3) and four different crustal thickness models. a) Top panel shows crustal thickness model of Schmandt et al., (2015). Following panels below top panel show χ^2 misfit map results when using crustal thickness in (a) as input to the BMMC inversion for cases 1-5, as labeled. Mean χ^2 misfits of the map area are given in the upper left portion of each map. Misfit map results in (a) are the same as what is shown in figure 4 but are shown again here for comparison. (b, c) Same as (a) but for the crustal thickness model of Shen et al., (2016), Buehler and Shearer, (2017), respectively. (d) Similar to (a-c) but local crustal thickness from Litherland and Klemperer, (2017) are only available beneath stations from the RMSE array. Dashed lines in (c) demarcate the area shown in (d). Inversion cases 4 and 5 achieve similarly low χ^2 misfits across all crustal thickness model inputs. Distribution and magnitude of χ^2 misfit are similar regardless of the choice of crustal thickness model.

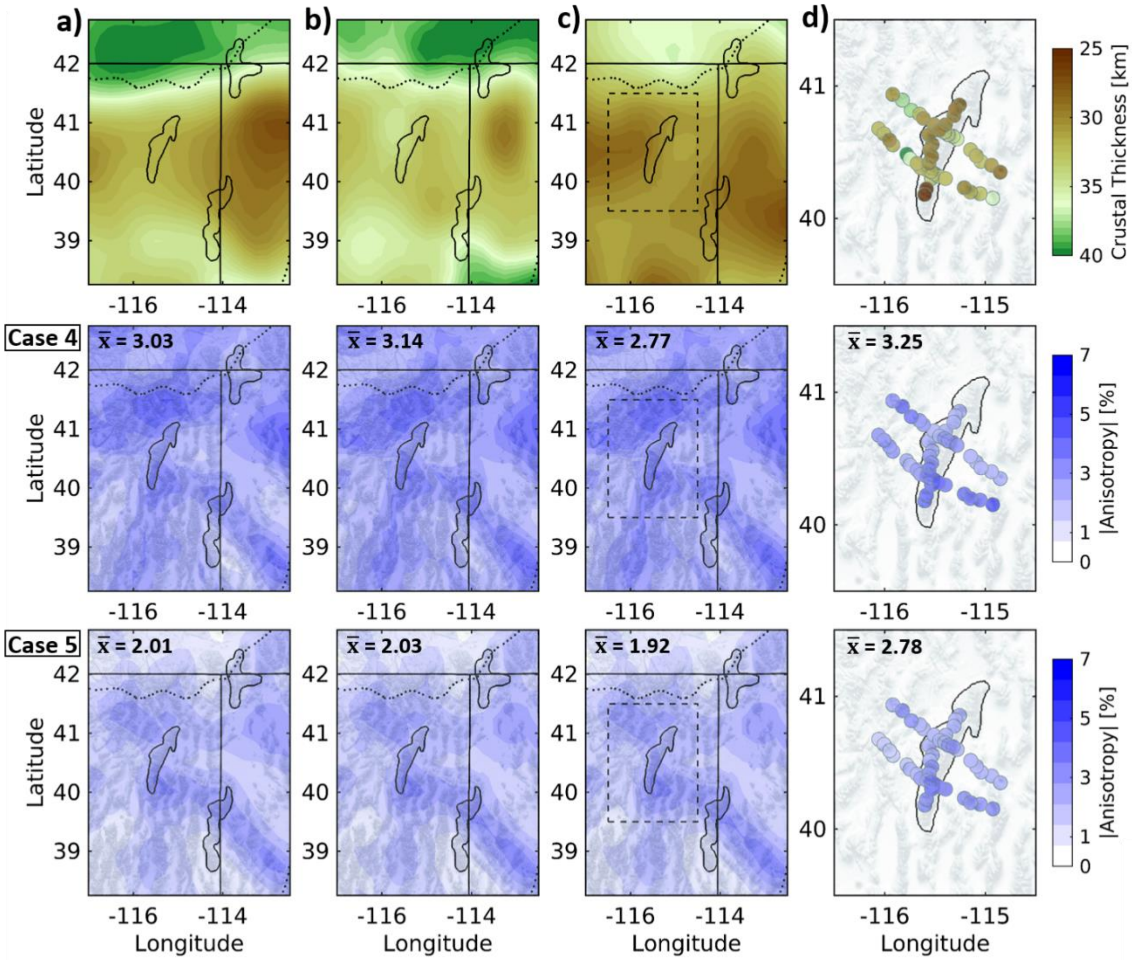

Figure S5. Same as figure 6 but including depth-integrated absolute value of crustal radial anisotropy from inversion cases 4 (also shown in fig 6) and 5 for comparison. a) The top panel shows the crust thickness model of Schmandt et al., (2015) and panels below top panel show depth-integrated absolute value of radial anisotropy when using crustal thickness in (a) as input to the BMMC inversion for inversion cases 4 (center) and 5 (bottom). Mean radial anisotropy of the map area ($\bar{x}$) is given in the upper left portion of each map. (b,c) Similar to (a) but showing results using the crustal thickness models of Buehler and Shearer, (2017) and (c) Shen and Ritzwoller, (2016), respectively. (d) Similar to a-c except local crustal thickness results from Litherland and Klemperer, (2017) are only available beneath stations from the RMSE array. Dashed lines in (c) demarcate the area shown in (d). Although the distribution of depth-integrated absolute value of crustal radial anisotropy are similar between inversion cases 4 and 5 there is a reduced magnitude of anisotropy in inversion case 5 relative to inversion case 4.

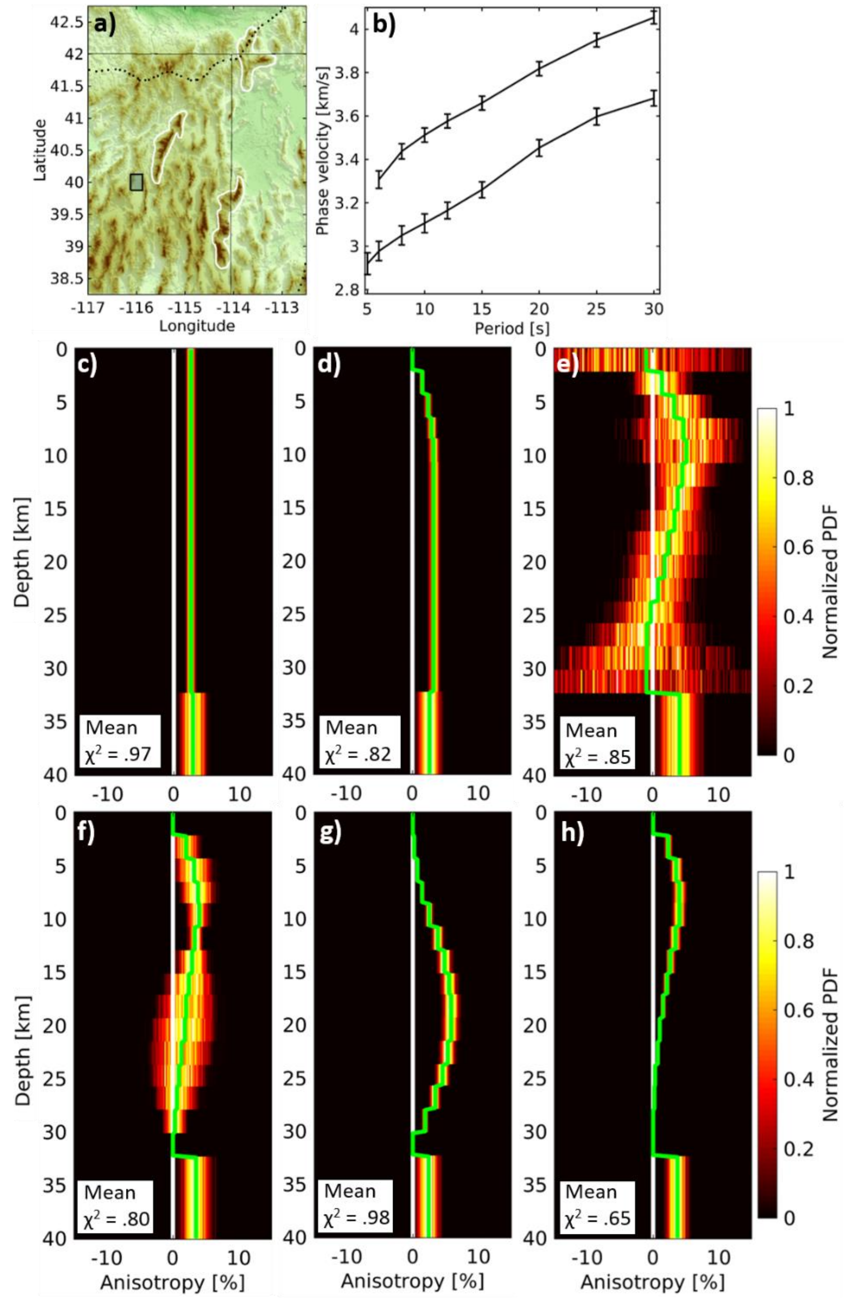

Figure S6. Effects of varying BMMC inversion parameterizations on posterior probability distribution of radial anisotropy as a function of depth from 1-D grid point 40°, -116°, the same grid point used by Moschetti et al., 2010a. (a) Map showing the location of grid point area (black box) and (b) associated dispersion curves and errors. Green lines are the mean of the posterior distribution. Mean χ^2 misfits for each case are given in the left portion of each panel. (c) Forced velocity increase with increasing depth, and an assumption of uniform radial anisotropy through the entire crust (similar to Xie et al., 2015). (d) Forced isotropy in the upper crust, forced increase in velocity with increasing depth, and equalized anisotropy in the middle and lower crust (similar to Moschetti et al., 2010a). (e) Parameterizations from inversion case 4. (f) Parameterizations from inversion case 5. (g) Allowing only b-spline 3 to be anisotropic in the crust. (h) Allowing only b-spline 2 to be anisotropic in the crust. The half-space mantle parameter is allowed to be anisotropic and this parameter is consistent throughout all of the inversion cases. All cases use the crustal thickness model of Schmandt et al., (2015).

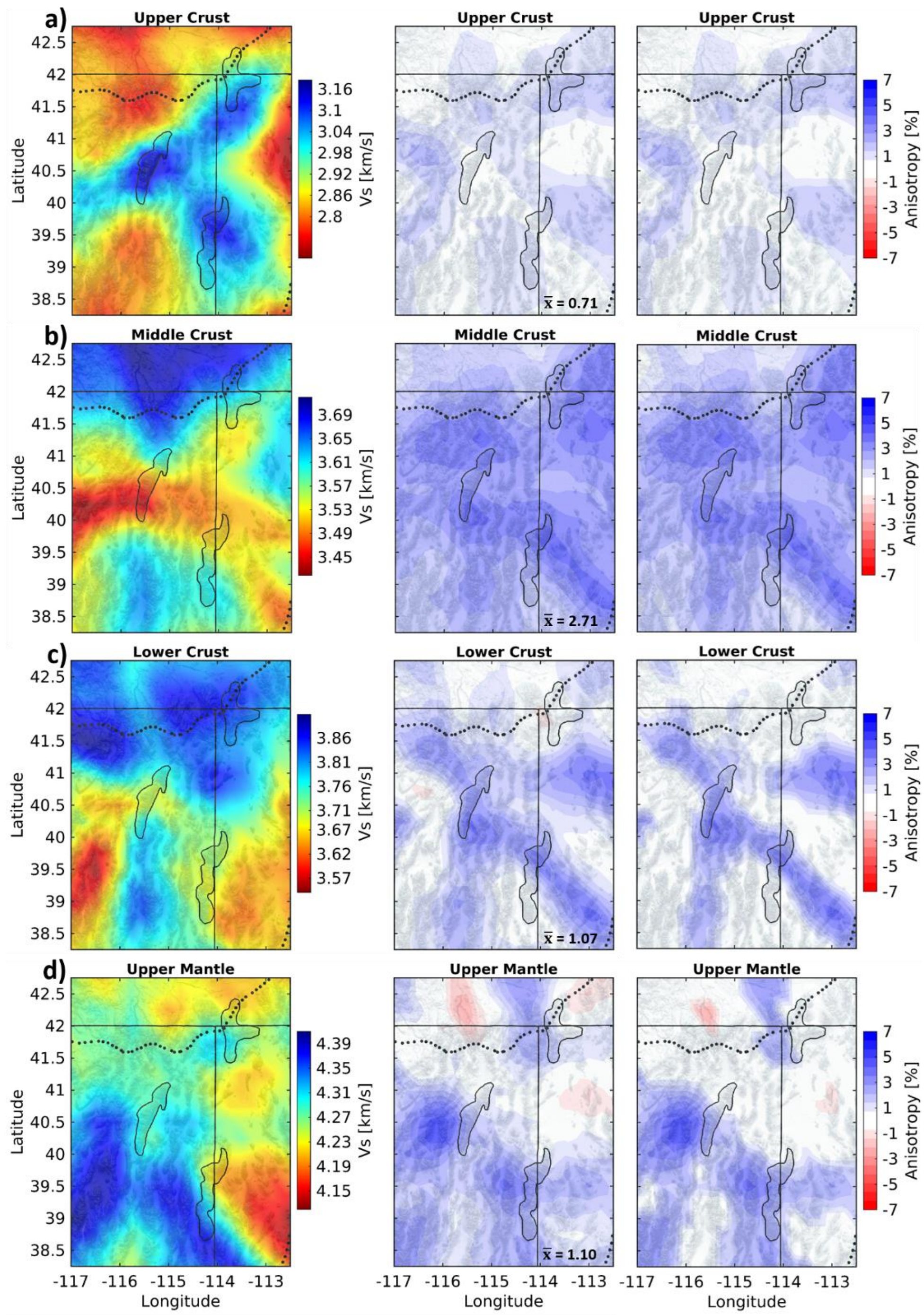

Figure S7. Same as Fig. 7 but for inversion case 5. Depth averaged isotropic V_S and radial anisotropy maps for the upper crust, middle crust, lower crust, and upper mantle. (a) Depth averaged isotropic V_S and radial anisotropy of the upper crust. Left panel shows isotropic velocity. Middle panel shows radial anisotropy results. The mean radial anisotropy of the map area ($\bar{x}$) is given in the lower right corner. Right panel shows only reliable results that have an absolute value of radial anisotropy greater than one standard deviation of the posterior. The upper crust maps average results between 0 and 5 km while the extent of depth averaging of the middle and lower crust is determined by evenly splitting the remaining thickness between 5 km and the Moho at each inversion point. (b-d) Same as (a) but for the middle and lower crust and upper mantle, respectively. All results shown in this figure are from inversion case 5 and correspond to inversions assuming the regional crust thickness model of Schmandt et al., (2015).

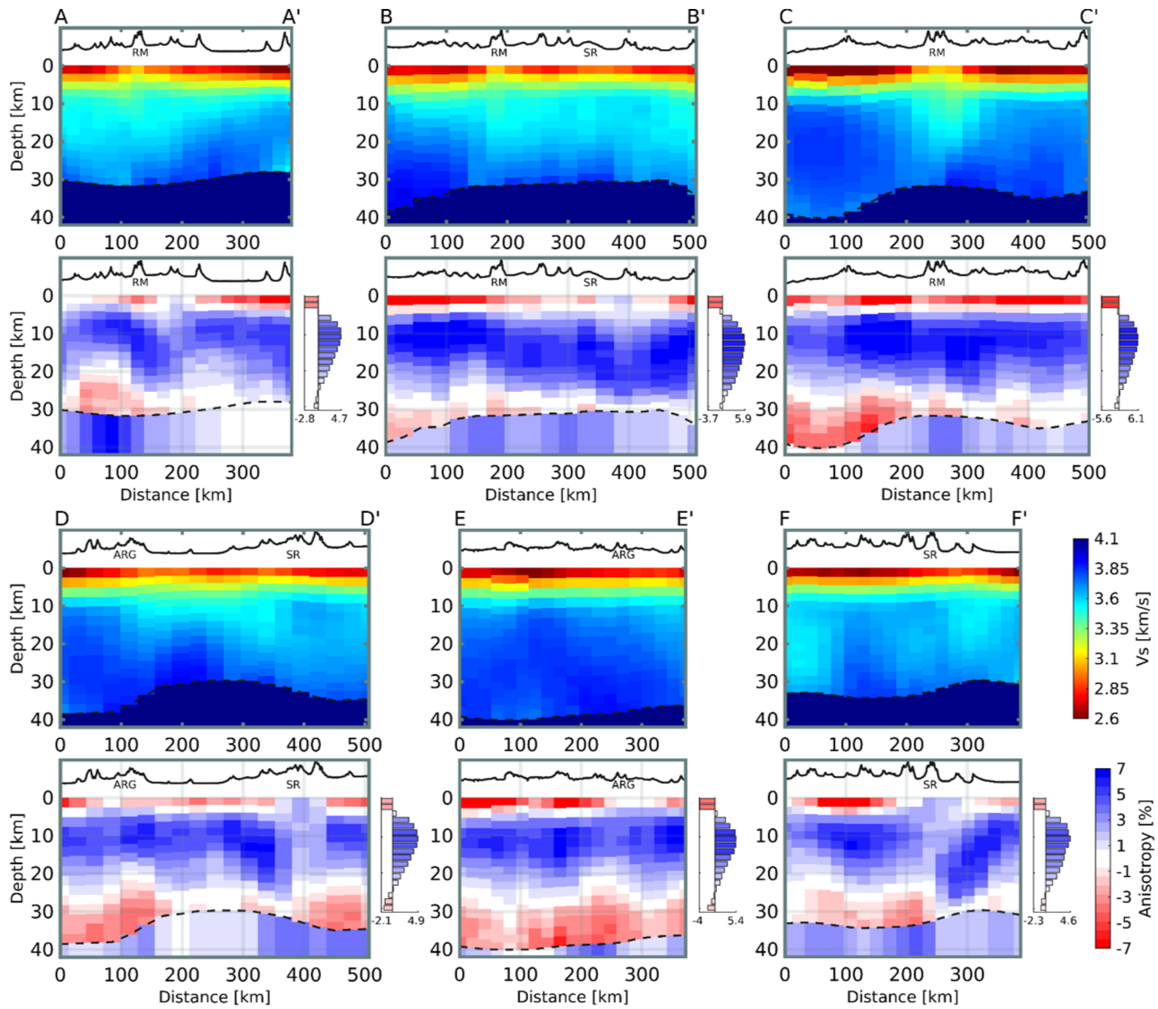

Figure S8. Same as figure 8, but showing isotropic V_S and anisotropy cross sectional (see figure 1) results from inversion case 4 without any statistical culling. Bar charts right of anisotropy cross-sections show average anisotropy profiles with depth for each cross-section. Anisotropy minima and maxima are labeled on the x-axis of each profile and colors correspond to anisotropy color bar. All panels shown here use the crustal thickness (dashed line) model of Schmandt et al., (2015). Topography is exaggerated 3 times in the profiles at the top of each panel.

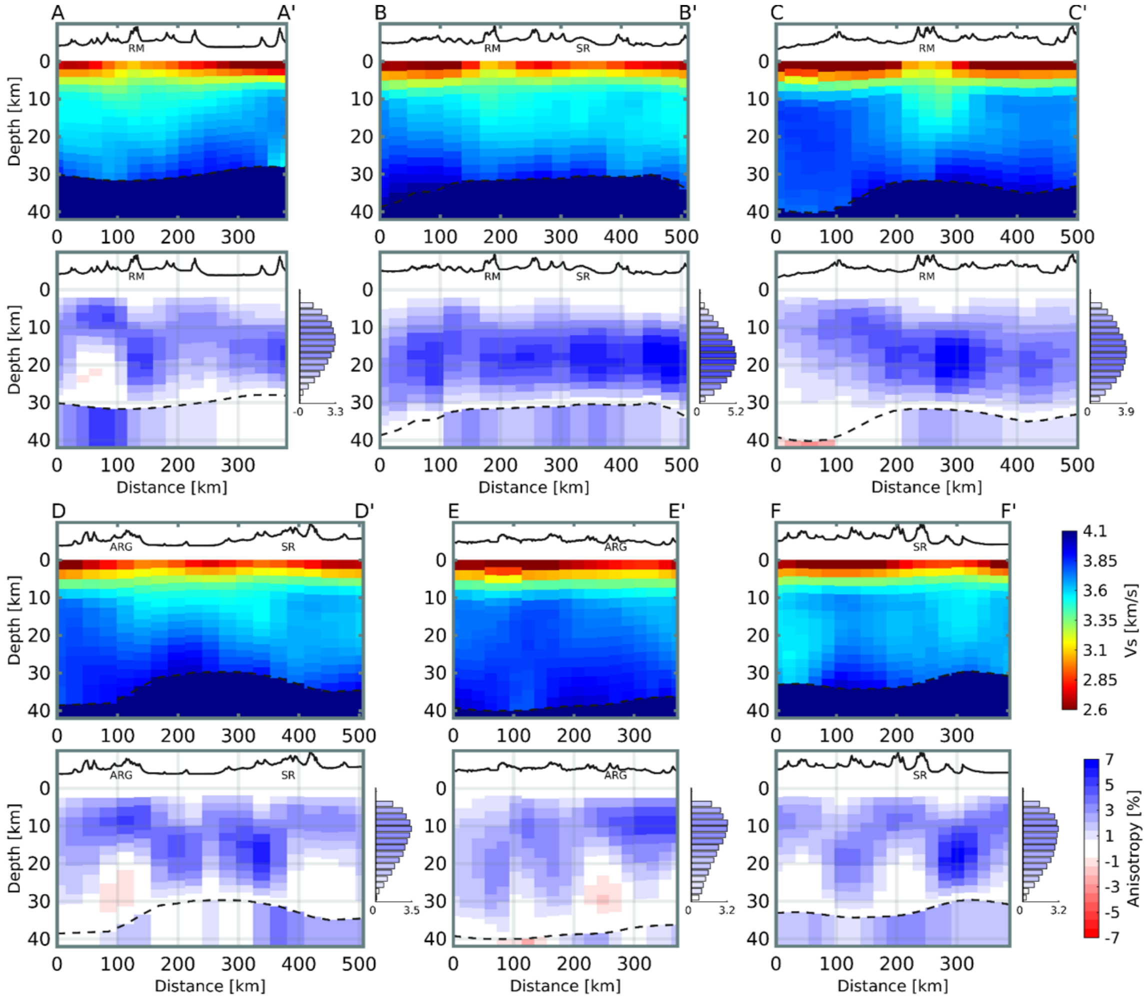

Figure S9. Same as figure 8, but showing isotropic V_S and anisotropy cross sectional (see figure 1) results from inversion case 5 without any statistical culling. Bar charts right of anisotropy cross-sections show average anisotropy profiles with depth for each cross-section. Anisotropy minima and maxima are labeled on the x-axis of each profile and colors correspond to anisotropy color bar. All panels shown here use the crustal thickness (dashed line) model of Schmandt et al., (2015). Topography is exaggerated 3 times in the profiles at the top of each panel.

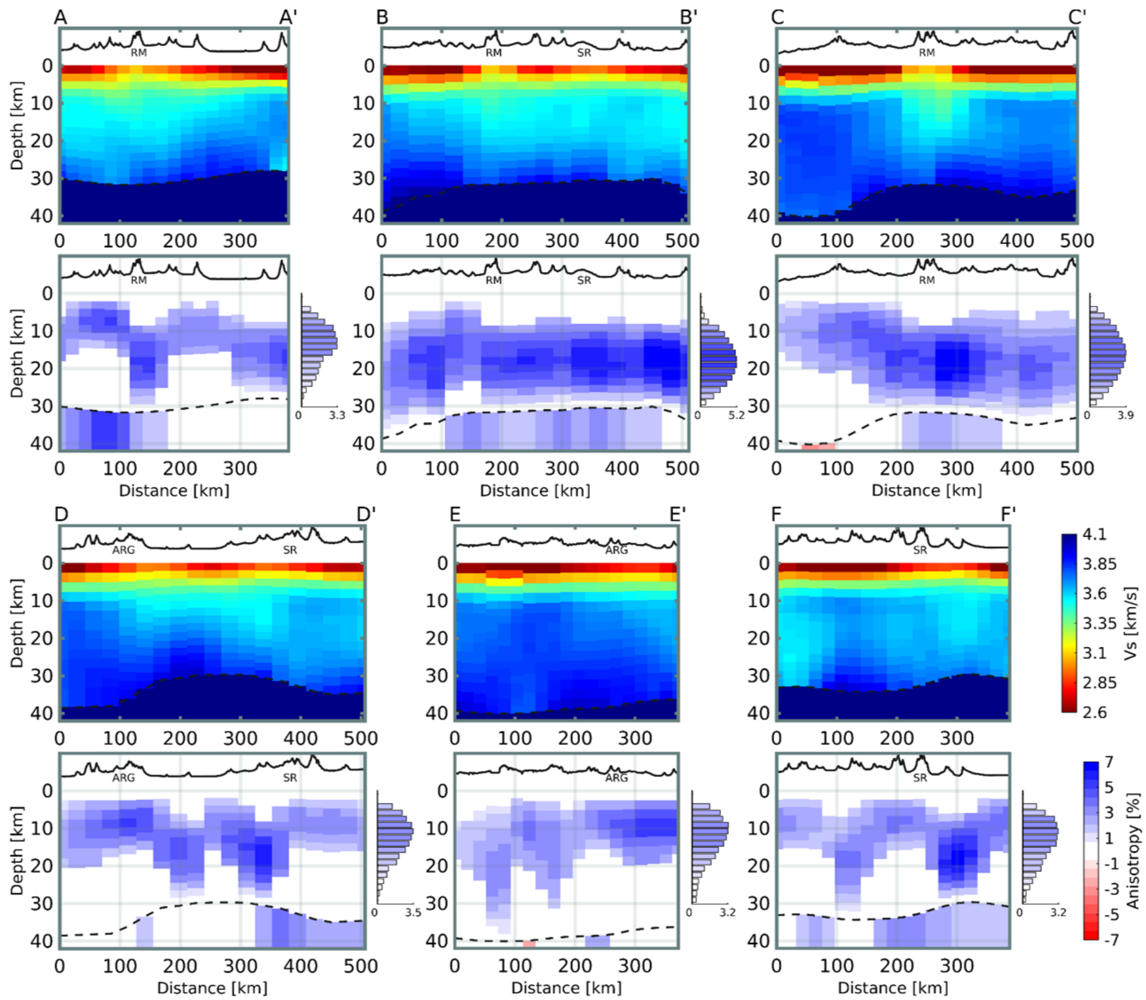

Figure S10. Same as figure 8, but showing only isotropic V_S and anisotropy cross sectional (see figure 1) results from inversion case 5 that have an absolute value of radial anisotropy with a significance greater than one standard deviation of the posterior distribution. Bar charts right of anisotropy cross-sections show average anisotropy profiles with depth for each cross-section. Anisotropy minima and maxima are labeled on the x-axis of each profile and colors correspond to anisotropy color bar. All panels shown here use the crustal thickness (dashed line) model of Schmandt et al., (2015). Topography is exaggerated 3 times in the profiles at the top of each panel.

Seismic network	DOI
TA	https://doi.org/10.7914/SN/TA
YX (RMSE)	https://doi.org/10.7914/SN/YX_2010
BK	https://doi.org/10.7932/BDSN
CI	https://doi.org/10.7914/SN/CI
IW	https://doi.org/10.7914/SN/IW
LB	N/A- http://www.fdsn.org/networks/detail/LB/
US	https://doi.org/10.7914/SN/US
UU	https://doi.org/10.7914/SN/UU

Table S1. Summary of seismic networks used for this study.

Period	Rayleigh error	Love Error
5	.050	-
6	.045	.040
8	.044	.035
10	.043	.033
12	.038	.032
15	.037	.032
20	.038	.033
25	.039	.032
30	.036	.029

Table S2. Rayleigh and Love wave errors at periods 5-30 s following Jiang et al., (2018).